Icarus 318 (2019) 42–55

Contents lists available at ScienceDirect

Icarus

journal homepage: www.elsevier.com/locate/icarus

Elemental composition and mineralogy of Vesta and Ceres: Distribution and origins of hydrogen-bearing species

T.H. Prettyman[a,*], N. Yamashita[a], E. Ammannito[b], B.L. Ehlmann[c,i], H.Y. McSween[d], D.W. Mittlefehldt[e], S. Marchi[f], N. Schörghofer[a], M.J. Toplis[g], J.-Y. Li[a], C.M. Pieters[h], J.C. Castillo-Rogez[i], C.A. Raymond[i], C.T. Russell[j]

[a] Planetary Science Institute, Tucson, AZ, USA
[b] Italian Space Agency, Rome, Italy
[c] California Institute of Technology, Pasadena, CA, USA
[d] University of Tennessee, Knoxville, TN, USA
[e] NASA Johnson Space Center, Houston, TX, USA
[f] Southwest Research Institute, Boulder, CO, USA
[g] CNRS/IRAP, University of Toulouse, Toulouse, France
[h] Brown University, Providence, RI, USA
[i] NASA Jet Propulsion Laboratory, California Institute of Technology, Pasadena, CA, USA
[j] University of California Los Angeles, Los Angeles, CA, USA

ARTICLE INFO

Article history:
Received 3 January 2018
Revised 26 April 2018
Accepted 27 April 2018
Available online 20 June 2018

ABSTRACT

Combined analyses of the surface elemental composition and mineralogy of Vesta and Ceres provide insights into their interior evolution, crustal formation, and regolith processes. Compositional data acquired by Dawn's Visible to Infrared Mapping Spectrometer (VIR) and Gamma Ray and Neutron Detector (GRaND) are sensitive to different depths and spatial scales. To compare these data sets, high-resolution maps of absorption band strengths from VIR are degraded to the broad spatial scales sampled by GRaND using a physics-based smoothing algorithm that accounts for the shape and topography of Vesta and Ceres. On Vesta, the distributions of elemental hydrogen and hydroxyl are similar, which implies that hydrogen is primarily in the form of hydroxyl, likely as phyllosilicates delivered by the infall of carbonaceous chondrite impactors. Small differences in the spatial patterns of hydroxyl and hydrogen imply that hydrogen is layered in some locations. In Vesta's dark hemisphere, hydrogen deposits are more extensive than hydroxyl, which indicates higher concentrations of hydrated minerals at depth. In contrast, the distributions of elemental hydrogen and hydrogen-bearing species (OH and NH_4^+) on Ceres are dissimilar. High concentrations of hydrogen in the Ceres' polar regions (approaching 30 wt.% equivalent H_2O) indicate the presence of subsurface ice as predicted by ice stability theory. The concentration of iron follows a water-dilution trend when plotted as a function of regolith hydrogen content, consistent with the presence of subsurface water ice. The VIR and GRaND data jointly constrain aspects of Ceres' surface chemistry and evolution. GRaND iron measurements place a firm upper bound on magnetite content, which supports graphitized carbon as an alternative to magnetite as a darkening agent. Lower-bounds on the concentration of carbon in carbonates implied by VIR, together with the ratio of carbonates to organics in carbonaceous chondrite meteorite analogs suggest high concentrations of carbon within Ceres' regolith. GRaND neutron measurements permit elevated carbon concentrations, equal to or in excess of that found in CI chondrites (greater than a few wt.%). Organic matter, detected by VIR at Ernutet crater, might be widespread and may have been converted to graphite, e.g. via UV exposure, elsewhere on the surface. Furthermore, elevated concentrations of carbonaceous material can explain the difference between iron and hydrogen concentrations measured by GRaND and the CI carbonaceous chondrites, which are representative of the materials from which Ceres accreted. The elemental measurements indicate that ice and rock fractionated during Ceres' evolution producing a crust that differs in composition from the whole body.

* Corresponding author.
E-mail address: prettyman@psi.edu (T.H. Prettyman).

https://doi.org/10.1016/j.icarus.2018.04.032
0019-1035/

1. Introduction

Over the past decade, the NASA Dawn mission has explored the two most massive asteroids in the main belt, Vesta and Ceres, determining their interior structure, geology, mineralogy and elemental composition (Russell et al., 2012;2016). On the way, Dawn acquired elemental data during a close flyby of Mars (Prettyman et al., 2011), enabling direct comparison of three solar system bodies. Dawn's Framing Camera (FC) (Sierks et al., 2011) and Visible to Infrared Mapping Spectrometer (VIR) (De Sanctis et al., 2011) provided high resolution mapping of geomorphology and mineralogy with nearly global coverage at Vesta and Ceres. Dawn's Gamma Ray and Neutron Detector (GRaND) (Prettyman et al., 2011) globally mapped the elemental composition of Vesta and Ceres providing constraints on their geochemical evolution.

The compositional information acquired by Dawn's instruments is complementary (e.g. Pieters et al., 2011); however, there are some technical issues that must be considered when combining optical and nuclear data sets. VIR is sensitive to surface and regolith geotechnical properties and mineralogy; whereas, GRaND is sensitive to the elemental composition of the bulk regolith. Model-based interpretation of nuclear spectroscopy data can in some cases provide constraints on regolith thermophysical properties, e.g. grain size and/or porosity (e.g. Boynton et al., 2002; Tokar et al., 2002; Prettyman, 2004; Prettyman et al., 2017). Joint analyses of optical and nuclear data must consider the completeness of the information provided and the disparate depth sensitivities and spatial scales of the measurements.

With reflectance spectroscopy, specific mineral species can be identified and in some cases quantified via the position and depth of absorption bands in the spectrum of sunlight reflected from the outermost layer of the surface (up to several hundred μm depth) (e.g. Hapke, 1981). Nuclear spectrometers detect gamma rays and neutrons produced by the steady interaction of cosmic rays with planetary surfaces and gamma rays made by the decay of natural radioelements such as K, Th, and U (e.g. Prettyman, 2014). The intensity and energy distribution of emitted radiation can be analyzed to determine the depth-averaged concentration of selected elements up to a few decimeters depth. The different depths sensed by the instruments can enable the detection and characterization of compositional layering; although, geochemical analyses are complicated when layering is present.

Remote sensing is selective in that not all elements and minerals present on the surface produce unique signatures that can be detected and quantified. Many complementary sources of information are required to determine surface composition. For example, the analysis and interpretation of nuclear spectroscopy data is guided by models of elemental composition based on theory and observations, including constraints from reflectance spectroscopy, meteorite and sample studies. Similarly, elemental data constrain the type and concentration of minerals within the regolith.

Dawn acquired data in circular polar mapping orbits around Vesta and Ceres. VIR spectra were acquired in high altitude mapping orbits with spatial resolution better than about 1 km/pixel (e.g. Ammannito et al., 2015;2016). GRaND data were acquired in a low altitude mapping orbit (LAMO), with an altitude of approximately 0.8 body radii at both Vesta and Ceres (Prettyman et al., 2012;2017). The angular response of GRaND's primary gamma ray and neutron sensors is described by Prettyman et al. (2011). GRaND is sensitive to radiation arriving from all directions. Consequently, the surface spatial resolution is a sizeable fraction of the field of view, the portion of the asteroid visible from the spacecraft that extends to the limb. In LAMO, GRaND can resolve compositional variations between surface regions hundreds of kilometers in scale, enabling characterization of only the largest impact basins and surface features. In order to compare GRaND and VIR mapping data, the VIR maps must be degraded to the spatial resolution of GRaND. This is accomplished here using a physics-based smoothing algorithm, which enables accurate comparisons of the two data sets.

This study compares the concentration and distribution of hydrogen with maps of hydrated minerals on Vesta and Ceres, with the goal of determining the types of hydrogen-bearing species present in the regolith and how they were emplaced. Vesta and Ceres are complementary protoplanets (Russell et al., 2004). Vesta formed inside the snow line of the solar nebula, accreted from a volatile-poor source (e.g. Hans et al., 2013; Prettyman et al., 2015), and underwent igneous differentiation, forming an iron-rich core, ultramafic mantle, and basaltic crust (e.g. Righter & Drake, 1997; McSween et al., 2011; Mandler & Elkins-Tanton, 2013; McSween et al., 2013; Toplis et al., 2013). Hydrogen-bearing species found on Vesta's surface are most likely exogenic (e.g. De Sanctis et al., 2012a; McCord et al., 2012; Prettyman et al., 2012). In contrast, water-rich Ceres formed outside the snow line and underwent extensive aqueous alteration. Ceres' regolith contains water ice, carbonates, organics, phyllosilicates, and other aqueous alteration products (e.g. Lebofsky et al., 1981; King et al., 1992; Rivkin et al., 2010; De Sanctis et al., 2015b; Ammannito et al., 2016; De Sanctis et al., 2017; Prettyman et al., 2017). By studying the elemental composition and mineralogy of Ceres' regolith, we can better understand interior evolution, crustal emplacement, and regolith processes. Combining VIR and GRaND data potentially enables the identification of subsurface components such as water ice and organics otherwise hidden from VIR (Prettyman et al., 2017).

This paper is organized as follows. The smoothing algorithm is presented in Section 2, along with an illustration of the spatial response function and a description of the data used in the study. The data include maps of the total inventory of hydrogen at Vesta and Ceres (GRaND), absorption band strengths for hydroxyl at Vesta and Ceres, and ammonium at Ceres (VIR). The distribution of iron on Ceres provides additional constraints on subsurface mineralogy. Comparisons of maps and their geochemical interpretation are provided in Section 3 and conclusions are presented in Section 4.

2. Methods and data

High-resolution maps determined from optical spectroscopy were degraded to the spatial resolution of GRaND using a physics-based, smoothing algorithm, which models the time series of counting data acquired by the instrument. The algorithm builds on a forward model described by Prettyman et al. (2017) that provides a detailed treatment of the emission of particles from the surface, their transport through space, and their detection by sensors in orbit. The model includes the shape and topography of Vesta and Ceres, which can affect how the instrument responds to surface features. The effect of shape is most important for Vesta (Prettyman & Hendricks, 2015), which is not in hydrostatic equilibrium and was battered into an irregular shape by large impacts (e.g. Jaumann et al., 2012; Marchi et al., 2012).

2.1. Forward model of GRaND measurements

For any location in orbit ($\vec{r}_D$), the response of GRaND to neutrons is given by a double integral over neutron kinetic energy (E) and the portion of the surface (S) visible from orbit (see Fig. 1A for an illustration of geometry and terms):

$$R\left(\vec{r}_D\right) = \kappa \int_S dA \int_E dE\ \varepsilon\left(-\hat{n}_D \cdot \hat{\Omega}, E\right) j\left(\vec{r}, E, \hat{n} \cdot \hat{\Omega}\right) e^{-t/\tau}/r^2 \quad \text{(counts/s)} \tag{1}$$

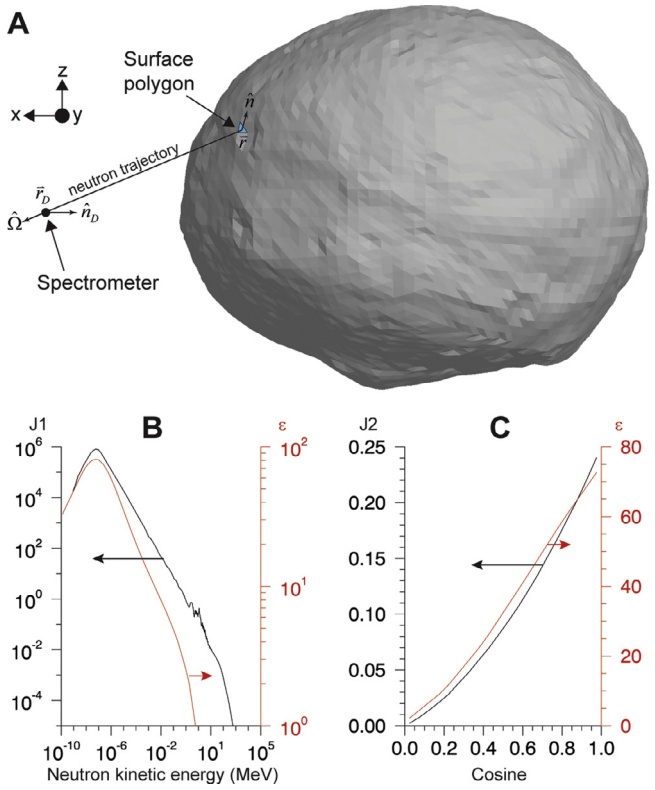

Fig 1. A) The trajectory of a single particle originating from the surface of Vesta and arriving at the orbiting spectrometer is illustrated. Terms in Eq. (1) are indicated. A polygonal shape model represents the surface. In B and C, surface emission and instrument response functions, respectively black (left axes) and red (right axes), are shown for neutrons produced by galactic cosmic ray interactions with howardite. B) The energy dependence of neutron emission integrated over all angles (vertical axis J1 with units of neutrons/cm^2/s/MeV) and the efficiency area product (ε) for detection of neutrons by the ^{6}Li(n,α) reaction in the Li-loaded glass scintillator, part of the +Z phoswich, for neutrons with normal incidence (red vertical axis, with units of cm^2) are shown. C) The angular dependence of the emitted neutrons and flux-weighted efficiency-area product are shown for neutron kinetic energies less than 100 keV. The horizontal axis gives the cosine of the angle of emission ($\hat{n}\cdot\hat{\Omega}$) or incidence ($-\hat{n}_D\cdot\hat{\Omega}$). The emission axis (J2) has units of neutrons/cm^2/s/steradian.

where κ is a constant, $j(\vec{r}, E, \hat{n}\cdot\hat{\Omega})$ is the steady-state leakage current of neutrons emitted in the direction $\hat{\Omega}$ from a surface parcel at $\vec{r}$ with unit outward normal $\hat{n}$ and area dA, $\varepsilon(-\hat{n}_D\cdot\hat{\Omega}, E)$ is the efficiency-area product (units of cm^2) of the sensor which is pointed in direction $\hat{n}_D$, and r and t are respectively the distance and transit time between the surface parcel and the sensor. Transit time depends on neutron kinetic energy. The model accounts for neutron decay (mean lifetime τ of about 900 s), but ignores gravitational binding effects (Prettyman et al., 2011). Thus, neutron trajectories follow straight-lines. For low altitude mapping orbits (LAMO) at Vesta and Ceres, neutron decay is only important for neutrons in the thermal energy range. In addition, because the spacecraft is moving slowly relative to Vesta and Ceres, we ignore kinematical ram effects. These simplifying assumptions were justified by Prettyman et al. (2013). Removing the exponential decay term from Eq. 1 gives the functional form for the response of GRaND to gamma rays.

Efficiency-area products were reported by Prettyman et al. (2011) for GRaND's primary neutron and gamma ray sensors. Multiplying the flux of incident particles (particles/cm^2/s) by the efficiency-area product (Fig. 1B) gives the contribution of the particles to the response (counts/s). Neutrons are detected by lithium- and boron-loaded plastic scintillators that face towards body center during science data acquisition. These are approximately planar in geometry, such that the projected area in the direction of the incident neutron varies roughly in proportion to $-\hat{n}_D\cdot\hat{\Omega}$, where $\hat{n}_D$ is the outward normal of the face of the scintillator (Fig. 1C). During science data acquisition, $\hat{n}_D$ points towards body center. Neutrons originating directly below the spacecraft, for which the projected area is largest, have higher probability of detection than those originating from the limb. Consequently, the neutron sensors yield slightly better spatial resolution than would be expected if the efficiency-area product were isotropic (i.e. independent of the direction of neutrons incident on the sensors).

The surface leakage current, with units of particles/cm^2/s/MeV/steradian, varies with the cosine of the polar emission angle $\mu = \hat{n}\cdot\hat{\Omega}$ (Fig. 1C). For gamma rays and neutrons produced in cosmic ray showers, emission is higher towards the zenith (e.g. $j \propto \mu^\alpha$ with $\alpha \cong 1.5$) (e.g. Lawrence et al., 2006; Prettyman et al., 2006; Eke et al., 2015), which enhances the response of the instrument to surface regions directly below the spectrometer in comparison to the special case of isotropic emission, for which $\alpha = 1$ (e.g. Prettyman et al., 2015). For cosmogenic neutrons and gamma rays, the anisotropy of emission is energy dependent. In this study, we used simulated leakage currents for analog materials to represent the energy-angle neutron emission functions for Vesta and Ceres.

Simulations of neutron emission were carried out using the Monte Carlo radiation transport code MCNPX, which models the particle showers produced by the interaction of galactic cosmic rays with the regolith (e.g. McKinney et al., 2006). For each analog material, the leakage current was determined for a flat surface parcel with an unobstructed 2π view of space. Shadowing of surface regions (e.g. by crater walls or mountains) and secondary scattering from reentrant surfaces was ignored. These effects are not expected to be significant (Prettyman & Hendricks, 2015).

For the purpose of smoothing, the composition of Vesta and Ceres was assumed to be spatially uniform. Vesta's composition was modeled as the howardite meteorite Kapoeta (Mittlefehldt, 2015), and the CI chondrite average composition was used for Ceres (Lodders and Fegley, 1998).

2.2. Smoothing of high resolution maps for comparison with GRaND data

Maps of any quantity $M(\vec{r})$ can be smoothed to the spatial resolution of GRaND by forming its footprint-weighted average. The smoothed map contribution at any point in orbit is given by $S(\vec{r}_D) = R_M(\vec{r}_D)/R(\vec{r}_D)$, where

$$R_M\left(\vec{r}_D\right) = \kappa \int_S dA \int_E dE\, M\left(\vec{r}\right)\varepsilon\left(-\hat{n}_D\cdot\hat{\Omega}, E\right) j\left(\vec{r}, E, \hat{n}\cdot\hat{\Omega}\right) e^{-t/\tau}/r^2 \quad \text{(map units} \times \text{counts/s)} \tag{2}$$

The integrals Eqs. (1) and (2) were evaluated numerically using the Monte Carlo importance-sampling scheme described in the Supplementary Material of Prettyman et al., (2017). The calculation was carried out for the time series of spacecraft orbital locations ($\vec{r}_D$) in LAMO that were used to make elemental maps at Vesta and Ceres. Evaluation of Eqs. (1) and (2) assumed GRaND was pointed towards body center, consistent with the measurement geometry for the selected orbital locations (Prettyman et al., 2012;2017). The time series of smoothed map values S was then binned onto equal area pixels with the same algorithms used for mapping measured counting rates, thus enabling direct comparison with GRaND maps. This process enables realistic modeling of nonuniform surface sampling (dithering) that may occur when binning map data.

Shape models of Vesta and Ceres were determined by stereophotoclinometry (SPC) using Framing Camera images and were represented by interconnected quadrilaterals (cubic topology) (Gaskell et al., 2008). For response calculations, the shape models were decimated to $16\times16\times16$ quadrilaterals and then converted

to polygonal (triangular) shape models. This ensures adequate subsampling of the surface, at scales much smaller than the footprint of GRaND, while minimizing computation time. For example, the shape model for Vesta is shown in Fig. 1A. The input maps $M(\vec{r})$ were projected onto the triangles for calculation of Eq. (2).

2.3. Solid angle approximation

Note that Eq. (1) is similar in form to the expression for the solid angle subtended by the surface at the spacecraft:

$$\Omega = \int_S dA\ \hat{n} \cdot \hat{\Omega}\ / r^2 \quad \text{(steradians)} \tag{3}$$

Counts (Eq. (1)) should vary in proportion to solid angle if the surface leakage current varies linearly with emission angle and the response of the spectrometer is independent of the angle of incidence. The assumption of solid-angle proportionality was made in geochemical mapping studies of Vesta and Ceres (Prettyman et al., 2012; Lawrence et al., 2013; Peplowski et al., 2013; Prettyman et al., 2013; Yamashita et al., 2013; Prettyman et al., 2017). For the purpose of correcting counting data for measurement geometry, the assumption is valid at LAMO altitudes (Prettyman and Hendricks, 2015), even though the aforementioned conditions are not strictly met.

The solid angle of an irregular shape is related to the equivalent altitude of the spacecraft in orbit around a sphere of the same volume as the shape model. Equivalent altitude (h_{eq}) is given by:

$$h_{eq}/R_{eq} = 1/\sqrt{1-(1-\Omega/2\pi)^2} - 1 \tag{4}$$

where R_{eq} is the radius of the equivalent-volume sphere. Solid angles and equivalent altitudes were archived in the NASA Planetary Data System for every measurement made by GRaND at Vesta and Ceres. The Monte Carlo simulations used to evaluate Eqs. (1) and (2) and are based on proven methods used to determine solid angle. The pipeline for calculation of Eq. 3 was validated by intercomparison of analytic, semi-analytic, and Monte Carlo calculations (Prettyman, 2017).

2.4. Visualization of the response function

In order to visualize the spatial response of GRaND, the solid angle and ^{6}Li(n,α) reaction rate (counts/s) were calculated for three discrete spacecraft locations at Vesta (Fig. 2A). At each location, the spacecraft was positioned 478 km from body center, which is approximately the average orbital radius for LAMO. The contribution of each surface element to the response, given by the integral over energy in Eq. 1, was tallied in the Monte Carlo simulation (Fig. 1A). Contributions to solid angle were also calculated (Eq. 3).

A map of the counting contributions (Fig. 2A) reveals the breadth of the footprint and sensitivity of GRaND to surface units. While regions closest to each subsatellite point make the largest contributions, only about 40% of the response originates within the full-width-at-half-maximum (FWHM) (e.g. the red-yellow region encircled by the dashed circle for location 3). The remainder originates from surroundings (blue). The patchy appearance of the map results from Vesta's irregular shape, with discontinuous regions as viewed from the spacecraft and variations in the projected area of individual triangles. The white arrow indicates a separate patch that belongs to the response at location 1. The extent of the footprint for location 2 at the South Pole is similar in scale to the Rheasilvia basin, which is nearly the diameter of Vesta.

The great circle indicated by the black arrows in Fig. 2A passes through each of the three locations. The distance from the spacecraft to the subsatellite point is compared with the solid-angle

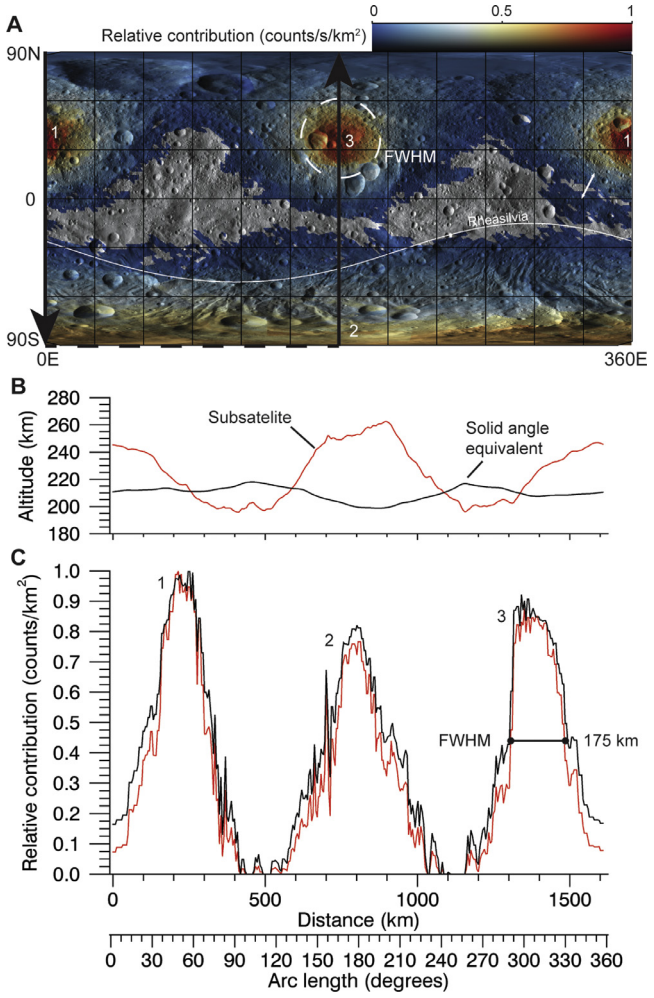

Fig. 2. A) The spatial response of GRaND is shown for three spacecraft subsatellite locations at Vesta: 1) 0E, 40 N; 2) 180E, 90S; and 3) 180E, 40 N. For each location (labeled 1–3), the distance of the spacecraft from body center was 478 km, roughly the average orbital radius for Dawn in LAMO. The contribution from surface parcels to the instrument response is indicated by a color map superimposed on shaded relief. Contributions from locations 1–3 were added together for illustration. A great circle that passes through the subsatellite locations is indicated by black arrows. The altitude of the spacecraft (subsatellite distance and solid-angle equivalent) is shown in B as a function of distance traveled on the surface along the great circle (horizontal axis shared with C). Surface contributions (normalized to the maximum for location 1) are shown in C. The black and red traces are respectively contributions to solid angle (Eq. (3)) and contributions to the instrument response (Eq. (1)). The selected locations are sensitive to separate surface regions. The white arrow in A indicates surface parcels associated with location 1. The full-width-at-half-maximum (FWHM), a measure of spatial resolution, is indicated for location 3.

equivalent altitude of the spacecraft (Eq. (4)) as a function of distance on the surface along the great circle (Fig. 2B). The orbital radius was fixed at 478 km. The subsatellite altitude depends on local topography of Vesta; whereas, the solid-angle equivalent altitude is sensitive to shape. Vesta's flattened shape fills more of the field of view near the poles than at the equator, despite that the subsatellite distance is larger at the poles. For Vesta's irregular shape, subsatellite altitude is not necessarily indicative of signal strength.

The width of the spatial response function can be determined by examining the relative contributions of surface units along the great circle (Fig. 2C). The black trace gives surface contributions to solid angle; whereas, the red trace gives contributions to the counting rate. The selected locations are sensitive to separate regions of Vesta's surface. The FWHM of the peaks associated with each of the three measurement locations provides a measure of

spatial resolution. Namely, two, identical point sources separated on the surface by the FWHM would meet Rayleigh's criterion for separation.

The spatial resolution of measurements with the lithium-loaded glass scintillator is somewhat better than the solid angle would indicate, primarily because neutron emission is enhanced in directions towards zenith (Fig. 1C); although, the instrument angular response and neutron decay also contribute. In addition, the peaks are narrower than would be expected given the rough approximation that the FWHM is 1.5 times altitude (Prettyman, 2014). For example, the FWHM of the peak at location 3 is 175 km, 40% lower than the approximate estimate (250 km). The approximation is based on the modeling of Apollo data acquired at much lower altitudes than LAMO (Haines et al., 1978) and is supported by studies of other low altitude data sets (Lawrence et al., 2003; Prettyman et al., 2009). As altitude increases, the FWHM-to-altitude ratio decreases due to the increased curvature of the surface as seen from orbit. Nevertheless, the rough approximation for resolution can serve as a useful guide. Surface features separated by less than about 200 km on Vesta and 400 km on Ceres in mapped counting data acquired at LAMO altitudes are difficult to distinguish.

The visualization shows that the spatial response of GRaND is not uniform for irregularly shaped bodies such as Vesta. The smoothing algorithm described here fully accounts for the shape of Vesta and Ceres, key aspects of the physics of particle production, transport, and detection, as well as the actual orbital trajectory flown by the spacecraft. This ensures accurate comparisons of high-resolution data sets and GRaND maps.

2.5. Map data

We compare the distribution of hydrogen-bearing mineral species measured by VIR to the distribution of hydrogen measured by GRaND at Vesta and Ceres. At Vesta, the strength of the 2.8 μm absorption band in reflectance spectra measured by VIR is sensitive to the concentration of OH-bearing minerals (De Sanctis et al., 2012a). In this study we use a map of the 2.8 μm band area, which provides coverage from the South Pole to roughly 60 N (Fig. 3A). See the Appendix for a description of the processing steps.

On Ceres, the signature for hydroxyl appears at 2.7 μm due to the prevalence of Mg-OH minerals, such as antigorite or saponite, which have absorptions at shorter wavelengths than Fe-bearing phases (De Sanctis et al., 2015b; Ammannito et al., 2016). Mg-phyllosilicates are more abundant than Fe-phyllosilicates in the most altered meteorites (CI and CM chondrites) (e.g. Howard et al., 2015; McSween et al., 2017). This implies that materials on Ceres' surface experienced a high degree of aqueous alteration. The band center does not vary significantly across the surface, which indicates that the composition of the phyllosilicates is relatively constant and implies that alteration was pervasive (Ammannito et al., 2016). De Sanctis et al. (2015b) also detected a 3.1-μm absorption feature, indicating the presence of ammoniated (NH_4^+) species, likely ammonium-bearing clays. Maps of OH and NH_4 band depths with coverage up to about 60° latitude in both hemispheres were derived from reduced data records (Level 1B PDS archive) using the same procedure as described in Materials and Methods of Ammannito et al. (2016), with the addition of data acquired in the High Altitude Mapping Orbit mission phase.

For comparison with GRaND data, high-resolution VIR maps were rebinned onto a 720×360 (0.5°) equirectangular grid and smoothed using the procedure described in Section 2. Pixels without map data were excluded from the evaluation of Eqs. (1) and (2). For illustration, the 0.5-degree basemap for OH on Vesta is shown in Fig. 3A. The smoothed time series was binned onto 15° and 20° quasi-equal area pixels (Gasnault et al., 2003), respectively, for Vesta and Ceres, the same grids used to map GRaND measurements (Prettyman et al., 2012;2017). Smoothed data were excluded from comparisons with GRaND data for regions without VIR coverage. For example, the smoothed map of VIR OH in Fig. 3B does not contain data poleward of 60 N.

At Ceres, we compare the global distribution of Fe to that of H and hydrogen-bearing minerals. A map of the concentration of Fe on 20-degree, quasi-equal area pixels was determined from measurements of the intense 7.6 MeV gamma ray produced by neutron capture with ^{56}Fe within the uppermost few decimeters of Ceres' regolith. The concentration of Fe within each map pixel was determined using the model-based, interpolation algorithm presented in the Supplementary Materials of Prettyman et al. (2017). The coupling between the subsurface neutron flux and capture gamma ray production was determined from measurements of neutrons in the thermal + epithermal energy range.

Absolute concentrations of H and Fe on Ceres were determined by comparison to measurements at Vesta, given assumptions regarding Vesta's average regolith composition. For the maps presented here, we assume the minimum concentration of hydrogen on Vesta determined by Prettyman et al. (2012). Meteorite studies support the validity of this assumption (Prettyman et al., 2012;2017). The elemental maps used in this study are sensitive to depth-averaged regolith composition.

3. Results and discussion

3.1. Vesta

The distributions of hydroxyl and H on Vesta are compared at the spatial resolution of GRaND in Fig. 3 (B and C, respectively). The patterns of H and OH are similar, with lowest values found in the relatively young, south-polar Rheasilvia impact basin (O'Brien et al., 2014; Schmedemann et al., 2014) and highest values in equatorial regions spanning roughly 60E to 210E, within Vesta's "dark" hemisphere (McCord et al., 2012; Reddy et al., 2012). This older, heavily cratered region is eucrite rich and may contain traces of Vesta's ancient, basaltic crust (De Sanctis et al., 2012b; Marchi et al., 2012; Ammannito et al., 2013; McSween et al., 2013; Prettyman et al., 2013). Dark materials are associated with eucrite rich regions (Palomba et al., 2014) and appear as areal deposits and localized spots and strata within the uppermost ~2-km of the surface (Jaumann et al., 2014). They contain OH in the form of phyllosilicates, such as serpentine, also found in CM and CR chondrites (e.g. Nathues et al., 2014). Although the exact delivery mechanism is debated, it is widely accepted that the dark, H-bearing materials are exogenic, delivered by the infall of carbonaceous chondrites, as impactors and/or dust (De Sanctis et al., 2012a; McCord et al., 2012; Prettyman et al., 2012; Reddy et al., 2012). The dearth of OH and H in the Rheasilvia basin implies that H-bearing materials were delivered prior to formation of the basin, likely early in Vesta's history following formation of the crust.

The howardite, eucrite, and diogenite (HED) meteorites probably originated from materials ejected by the impact that formed Rhesilvia (e.g. Schenk et al., 2012; Marchi et al., 2013). These include regolith materials, some of which contain solar wind gases, evidence that they were exposed on the surface (Cartwright et al., 2013;2014; Lunning et al., 2016). Some regolithic howardites contain carbonaceous chondrite clasts, evidence that Vesta's ancient surface was exposed to primitive, water-rich impactors (e.g. Prettyman et al., 2012, Supplementary Material). Low-velocity accretion of carbonaceous chondrites would have resulted in minimal alteration of phyllosilicates, preserving their hydrogen content. Indeed, estimates of the average hydrogen concentration of howardites with carbonaceous clasts are consistent with that measured by GRaND within Vesta's regolith, and delivery of H by the solar wind is thought to be negligible based on analyses of Ne iso-

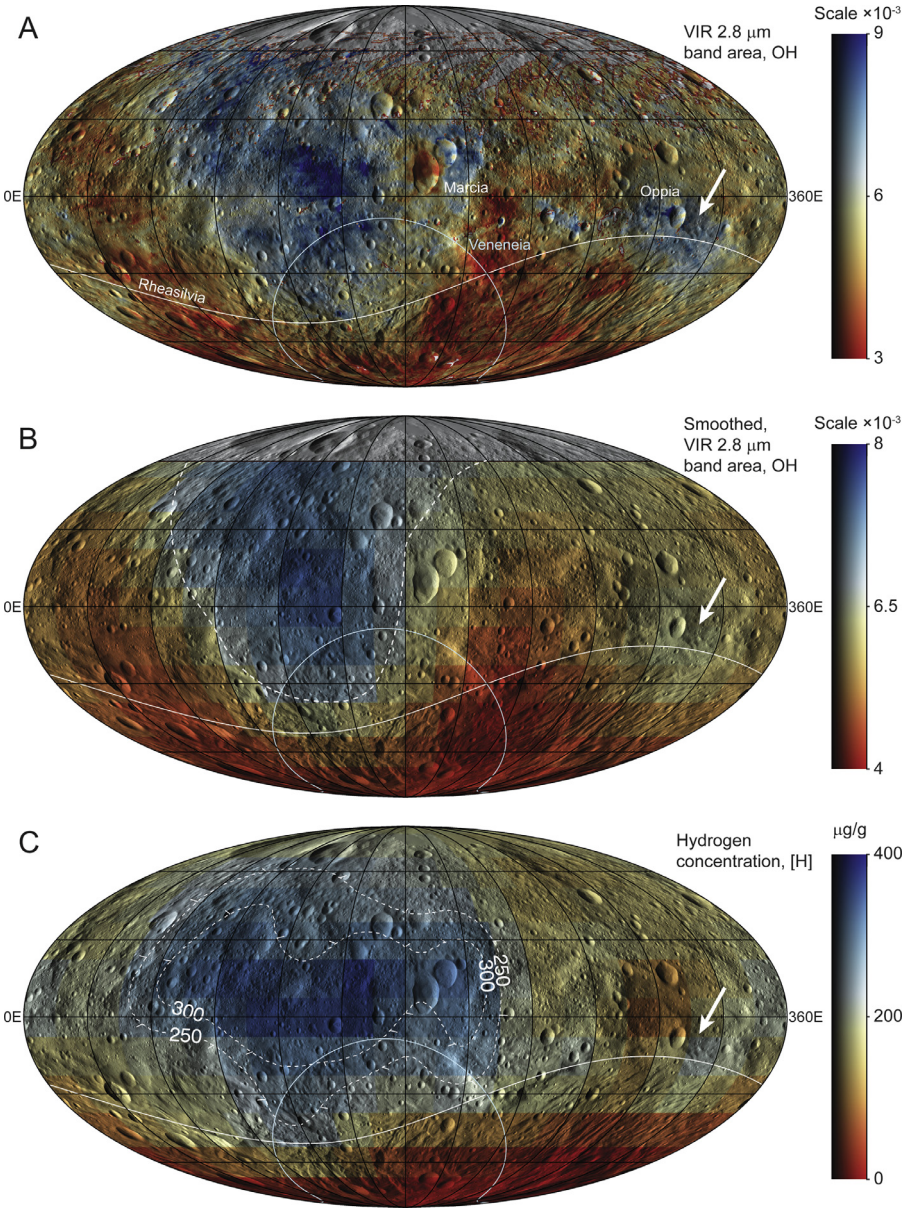

Fig. 3. Maps of Vesta. A map of the VIR 2.8 μm band area (A) before and (B) after smoothing to the spatial resolution of GRaND are compared to (C) a map of hydrogen measured by GRaND. Map data in (B) and (C) were binned on 15-degree quasi-equal-area pixels. For context, the map data (color scale) are superimposed on shaded relief. The maps are in the Claudia coordinate system (Russell et al., 2012). Outlines of the two largest impact basins are shown (white – Rheasilvia; blue – Veneneia). Arrows indicate the location of a medium albedo region with enhanced 2.8 μm absorption in and around Oppia crater. The largest band areas are found in the region highlighted by the dashed line in (B), which marks the transition from blue to yellow on the map. The same color transition is approximated by 250 μg/g contour on the hydrogen map in C.

topes (Prettyman et al., 2012). In addition, VIR observations are inconsistent with the formation of O–H bonds by the interaction of solar wind protons with the surface (De Sanctis et al., 2012a).

The strong correlation between GRaND and VIR map values shown in Fig. 4 suggests a causal relationship between H and OH. This, of course, assumes that the concentration of OH varies in proportion to the 2.8 μm band area (Sato et al., 1997; De Sanctis et al., 2012a). If so, then we can assert that most of the hydrogen within Vesta's uppermost regolith is in the form of hydroxyl. The presence of H in other forms, such as bound or adsorbed water, may contribute to minor differences between the distribution of OH and H (Fig. 3B and C); however, bound water was not detected by VIR (De Sanctis et al., 2012a). Consequently, the differences may result from layering of hydrogen within the subsurface. VIR is sensitive to the uppermost few hundred μm of the surface; whereas, GRaND is sensitive to decimeter depths. Layering of dark deposits is observed on much larger scales, and it is reasonable to expect that layering could occur within the shallow depths sensed by GRaND and VIR. Nevertheless, the close correspondence between H and OH suggests that Vesta's regolith is generally not layered on the spatial scale of GRaND measurements. Possible exceptions are described as follows.

Perhaps the most noticeable difference in the smoothed maps is the shape of the hydrogen-rich regions in Vesta's "dark" hemisphere (compare dashed lines marking the transition from blue to yellow in Fig. 3B and C). The longitudinal extent of H is much greater than that of OH, which may imply higher concentrations of hydrogen beneath the optical surface in regions such as the ejecta

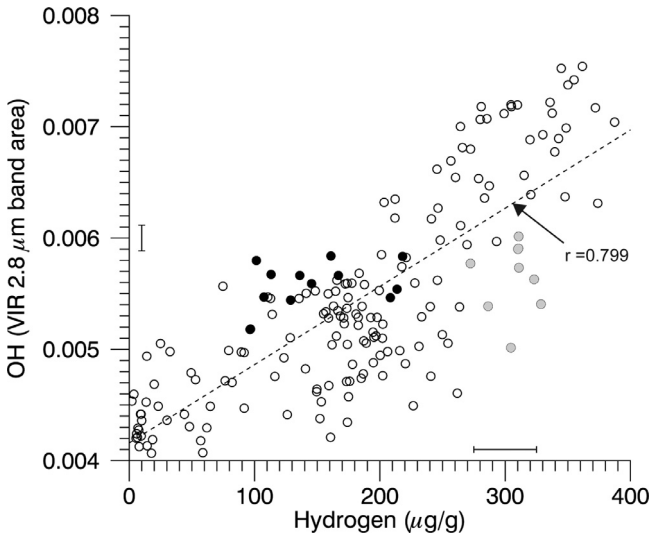

Fig. 4. Scatter plot of the VIR 2.8 μm band area, smoothed to the spatial resolution of GRaND, versus hydrogen concentration (map data for Vesta are shown in Fig. 3B and C). Values for 180 pixels south of 60 N are compared. A two-tailed *t*-test indicates the null hypothesis that the distributions of H and OH are unrelated can be rejected with high confidence. The critical t value for 178 degrees of freedom with 5% significance level is 1.97, which is much smaller than the value determined from the population (t = 17.7). Filled symbols (black) are for pixels in the vicinity of Oppia (region indicated by white arrows in Fig. 3). The region includes 12 pixels with latitudes between 37.5S and 7.5 N and longitudes between 285E and 345E. Filled symbols (light grey) are for pixels around and to the east of Marcia, with latitudes between 7.5S and 37.5 N and longitudes between 180E and 225E (9 pixels, two of which overlap on the plot). Error bars represent the uncertainty in individual data points. The error bar for the vertical axis gives the population standard deviation of the mapped values for each pixel. The horizontal error bar gives the total analytical uncertainty in the hydrogen concentration for individual pixels.

deposits to the east of Marcia crater (De Sanctis et al., 2015a), or that these "hidden," subsurface deposits have greater spatial extent than indicated by VIR. Relatively low 2.8-μm band areas are found for some pixels with intermediate to high concentrations of hydrogen (150- to 350-μg/g). Points in the vicinity and to the east of Marcia cluster below the regression line (Fig. 4), which could result from elevated concentrations of H at depth in the form of hydrated minerals or bound water. High concentrations of H and OH extend to the south into the Veneneia impact basin (the 250 μg/g H contour follows the outline of the basin rim, Fig. 3C). Reddy et al. (2012) speculate that much of the dark material to the north and west of Veneneia is ejecta from the impact of a carbonaceous asteroid, which formed the basin.

VIR detected hydroxyl to the south of Oppia crater (blue region indicated by arrow in Fig. 3A). In this region, the 2.8 μm band corresponds to materials with moderate reflectance, perhaps indicating that OH was emplaced there by a mechanism other than infall of carbonaceous chondrites, such as a cometary collision or an endogenic source (De Sanctis et al., 2012a; Scully et al., 2015). In the scatter plot of OH versus H (Fig. 4), points within this region cluster above the regression line, consistent with higher concentrations of OH on the surface than at depth. The inferred inverted layering is consistent with an exogenic source.

3.2. Ceres

The distribution of hydrogen on Ceres is strikingly different from that of Vesta. Whereas H on Vesta is longitudinally asymmetric (Fig. 3C), longitudinal variations on Ceres are small (Fig. 5A). The concentration of hydrogen within Ceres' regolith increases markedly with latitude, with slightly higher concentrations near the North Pole than the South Pole. Moreover, the average concentration of hydrogen on Ceres is hundreds of times higher than that of Vesta, reflecting an abundance of aqueously altered minerals, water ice, and other hydrogen-bearing molecules on Ceres.

The presence of subsurface ice can explain the high concentrations of H observed at high latitudes. Prettyman et al. (2017) argue that the increase in H with latitude indicates the presence of a global, subsurface ice table, consistent with predictions of ice stability modeling (Fanale and Salvail, 1989; Hayne and Aharonson, 2015; Titus, 2015; Schorghofer, 2016). Over billions of years, loss of ice by sublimation caused the gradual recession of the ice table from the surface to greater depths, with the highest losses occurring in warmer, equatorial regions. Assuming ice initially filled the pore space, the depth of the ice table varies from about a meter at the equator to within a few millimeters near the poles and contains on average about 10 wt.% water ice.

Long-term variations in illumination due to changes in Ceres' orbital elements cannot plausibly explain the observed north-south asymmetry in hydrogen (Prettyman et al., 2017). Instead, this asymmetry may result from differences in the excavation and redistribution of crustal materials by impacts. Much of the southern hemisphere was resurfaced by ejecta from large impacts (Marchi et al., 2016; Stephan et al., 2017; Strom et al., 2018).

Subsurface ice is widespread on the spatial scales sampled by GRaND (about 400 km resolution in LAMO). Small patches of surface ice are visible within high latitude craters (Combe et al., 2016; Combe et al., 2017) and in the mid-latitude crater Juling (Raponi et al., 2018). In addition, analyses of lobate flows show that their morphology is controlled by ice, perhaps in larger concentrations than inferred regionally from GRaND data (Schmidt et al., 2017). This suggests that the distribution of ice within the crust and regolith is heterogeneous on small scales (less than a few km). Further evidence for crustal ice includes pitted terrain made by rapid outgassing of the subsurface in response to impact heating (Sizemore et al., 2017). Surficial ice may be the source of the tenuous cerean exosphere detected by telescopes and GRaND (Kuppers et al., 2014; Formisano et al., 2016; Russell et al., 2016; Landis et al., 2017; Schorghofer et al., 2017; Villarreal et al., 2017).

The mineralogy of Ceres is consistent with extensive and pervasive aqueous alteration of silicate minerals. Ceres' global regolith as seen by VIR is rich in Mg-phyllosilicates, ammonium-bearing clays, carbonates, and a neutral, darkening agent such as magnetite or graphitized carbon (De Sanctis et al., 2015b; Ammannito et al., 2016). Ceres likely accreted unaltered silicate minerals, ice and other volatiles. The VIR data are consistent with an interior that was warm enough to melt ice, producing liquid water that altered the silicates to form Fe-serpentine, which was converted to Mg-serpentine, magnetite and clay minerals as alteration progressed (McSween et al., 2017).

Given that aqueous alteration is exothermic (e.g. Fyfe, 1974), serpentization and melting of ice propagate through the interior until the reactants are consumed (e.g. Bland and Travis, 2017). Ceres is large enough that silicates, alteration products and brine likely circulated within the interior (Bland et al., 2009). Elemental fractionation could have occurred if the more mobile brine separated from solid particulate (Neveu and Desch, 2015). Analyses of gravity and topography indicate that the interior of Ceres is physically differentiated and that in addition to phyllosilicates, the crust contains salt, salt-hydrates and/or clathrates, possibly the remnants of a subsurface ocean (Fu et al., 2017; Castillo-Rogez et al., in review).

Fig. 5 compares the distributions of hydrogen-bearing mineral species (OH and NH_4^+) measured by VIR within the uppermost 10s-100 s of μm of Ceres' surface with the total concentration of hydrogen measured by GRaND. When smoothed to GRaND's resolution, the VIR maps reveal higher concentrations of hydrogen-bearing species in the eastern hemisphere. The coherent pattern

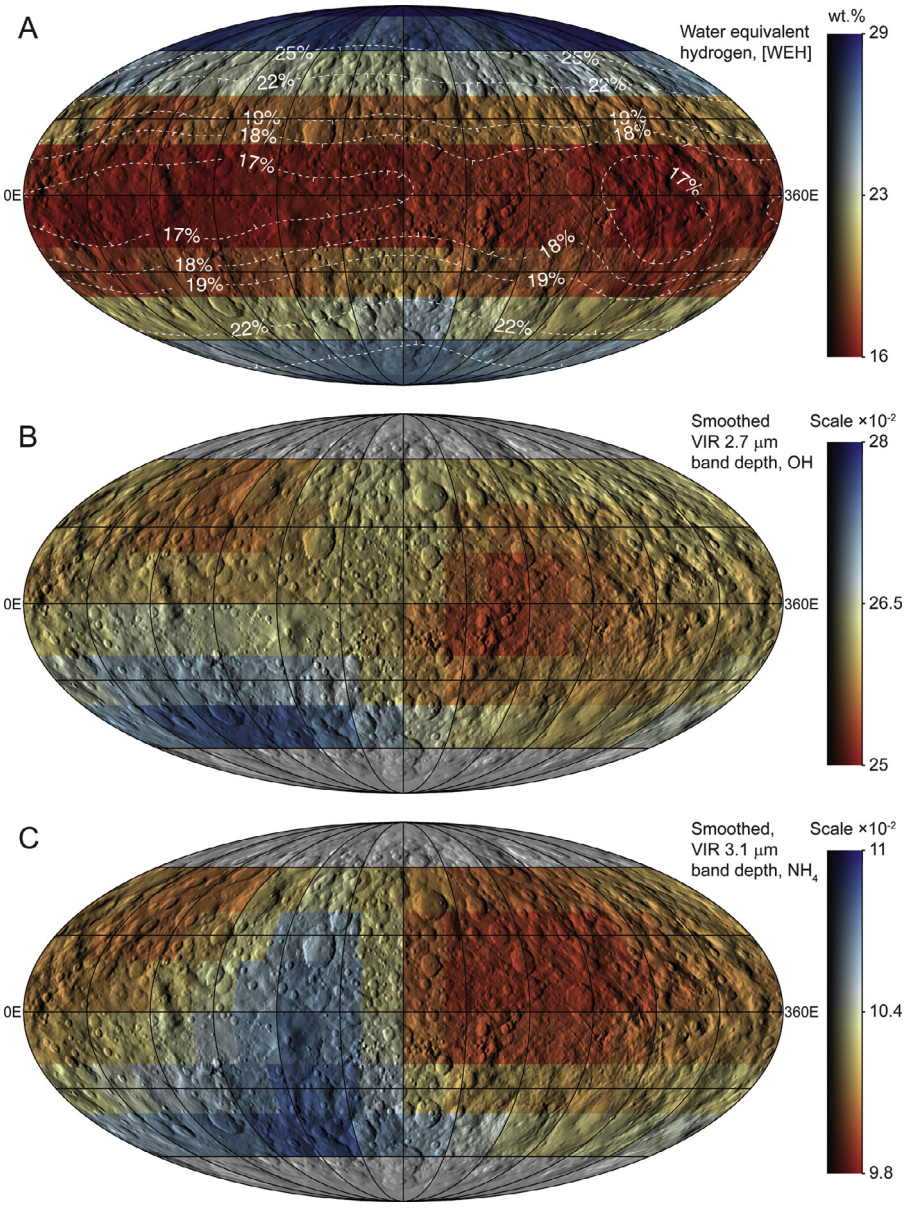

Fig. 5. Maps of Ceres. (A) The distribution of hydrogen on Ceres determined by GRaND is compared with smoothed maps of (B) the 2.7 μm band depth (OH) and (C) the 3.1 μm band depth (ammoniated species) by VIR. The map data (color on shaded relief) were binned on 20-degree quasi-equal area pixels. While hydrogen concentration is presented in terms of water equivalent hydrogen (WEH), hydrogen may take other forms such as ammonium and organics. The prime meridian passes through crater Kait (Roatsch et al., 2016).

of OH and NH_4^+ implies that they are borne by the same suite of minerals (Ammannito et al., 2016). The dynamic range of the VIR data, (max-min)/avg (about 12%), is small compared to the dynamic range of hydrogen from GRaND, which is 60%. The lack of ice in the thin layer sensed by VIR explains this difference.

GRaND measurements within 20° of the equator represent Ceres' ice-free regolith composition. In this region, the variation in the GRaND data is similar to the total analytical uncertainty in the hydrogen concentration for individual pixels, about 1 wt.% (Prettyman et al., 2017) (Fig. 6). Elements such as carbon can produce changes in neutron counts, which bias the determination of hydrogen. The absence of a positive correlation between hydrogen and hydrated mineral species for equatorial pixels (Fig. 6) hints at variability in regolith carbon content. Increasing the concentration of carbon decreases production and increases moderation of neutrons, which has a similar effect on neutron counting data as increasing the concentration of hydrogen (Prettyman et al., 2017). Consequently, slightly higher inferred concentrations of hydrogen within the equatorial band in the western hemisphere (Fig. 5A) could instead result from increased regional carbon concentrations.

Globally, OH and NH_4^+ are weakly correlated with H (Fig. 6). While the correlation between OH and H is statistically significant, the relationship is not causal due to the aforementioned uncertainty in ice-free regolith hydrogen content and the disparate depths sensed by GRaND and VIR. Both OH and H increase with latitude and the presence of subsurface ice explains the observed variation in bulk hydrogen. Changes in hydrated mineral content with latitude were anticipated prior to Dawn's arrival at Ceres, for example due to changes in the thermo-physical properties of the crust with latitude (McCord and Sotin, 2005; Castillo-Rogez and McCord, 2010); however, the observed variations in OH and NH_4^+ are subtle and support globally uniform processing and emplacement of materials on broad spatial scales.

Together with hydrogen, the distribution of iron within Ceres' regolith provides insight into the concentration of ice and al-

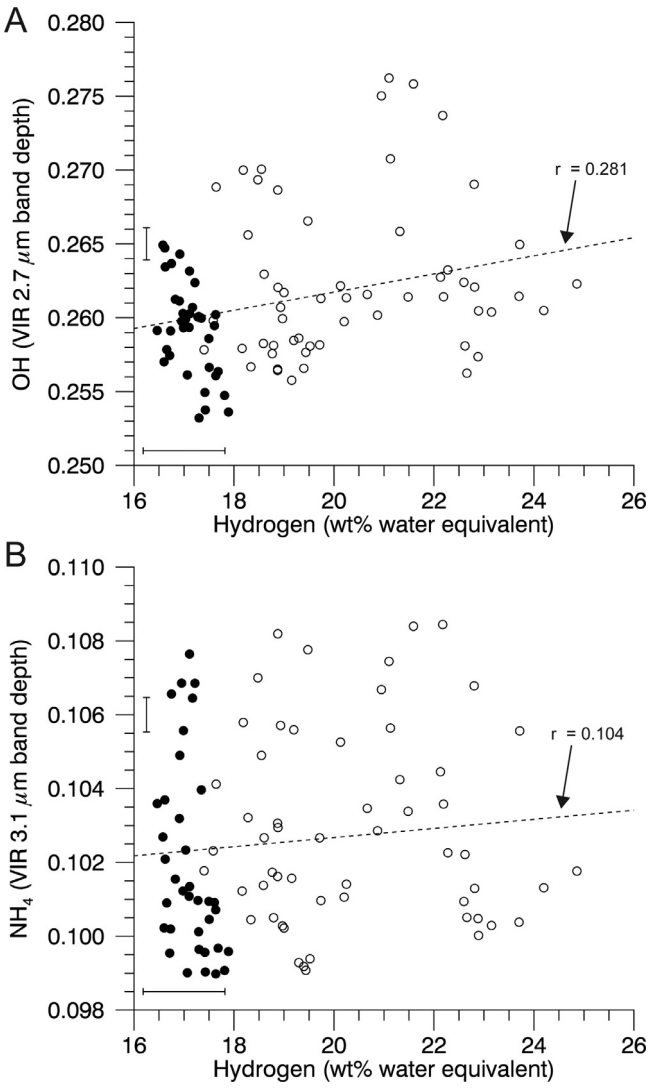

Fig. 6. Scatter plots of (A) the 2.7 μm band depth and (B) the 3.1 μm band depth versus hydrogen concentration. Each of the 92 points corresponds to a 20-deg equal area pixel from the maps of Ceres in Fig. 5. Pixels poleward of 60-degrees in the north and south are excluded. Global regression lines and Pearson correlation coefficients are shown. The correlation between H and the 2.7 μm band, although weak, is statistically significant (for r = 0.281 with 90 degrees of freedom, t is 2.778, which is larger than the critical value of 1.987 for 5% significance); whereas the slight positive correlation between H and NH_4 is not. Points equatorward of 20° latitude in the northern and southern hemisphere are filled (black). Error bars represent the uncertainty in individual data points. The error bars for the vertical axes give the population standard deviation of the mapped values for each pixel. The horizontal error bar gives the total analytical uncertainty in the hydrogen concentration for individual pixels, about 1 wt.%. The statistical contribution is small compared to the scatter in the equatorial data (Prettyman et al., 2017).

teration products, their origin, and emplacement (Fig. 7). Since the CI chondrites are representative of the solar nebula (e.g. Lodders, 2010), the composition of Ceres' ice-free regolith is expected to be similar to CI as long as ice-rock fractionation did not occur. In this respect, we note that the concentration of iron is lower than that of CI whole rocks, even when dilution by bound or adsorbed water is considered (Fig. 8, trend line a); although, some equatorial pixels approach the dilution line.

Carbon/carbonate mineralogy is another way in which Ceres and the CI meteorite analogs differ. For the aqueously altered chondrites, carbon is primarily in the form of insoluble organic matter (IOM), which likely originated in the nebula and/or interstellar space (e.g. Pizzarello et al., 2001). The carbon in IOM is incorporated into carbonates as alteration progresses within the parent body. Thus, the carbonate/organic mass ratio provides a measure of the degree of aqueous alteration (Alexander et al., 2013; Alexander et al., 2015; McSween et al., 2017). On Ceres, carbonates are widespread (De Sanctis et al., 2015b) and Na-carbonates are found in localized, bright deposits (De Sanctis et al., 2016). The 3.4 μm region that is characteristic of carbonates is complex and could also contain contributions from C–H bonds from 3.3–3.5 μm; however, the C–H bonds characteristic of aliphatic organic matter have been detected in only one small region partially overlapping Ernutet crater (Pieters et al., 2017; De Sanctis et al., 2017). The apparent dearth of organic molecules on Ceres' surface may result from weathering processes that graphitize carbon (Prettyman et al., 2017, Supplementary Material; Kaplan et al., 2018). In fact, the UV spectrum of Ceres appears to be dominated by an anthracite-like species (Hendrix et al., 2016), consistent with this idea.

Spectral mixing fractions for representative mineral end members were determined in an analysis of the global average spectrum acquired by VIR (De Sanctis et al., 2015b). These can be interpreted as areal- or volume-fractions, which can be converted to weight fractions given estimates of the density (ρ) of mineral components and the regolith (i.e., $\text{wt.\%} = \text{vol.\%} \times \rho_{\text{mineral}}/\rho_{\text{regolith}}$). In the analysis that follows, we used a regolith density of 1.8 g/cm^3, based on an assumed grain density of 2.2 g/cm^3, the minimum for CI chondrites reported by Britt and Consolmagno (2003) and a porosity of 0.2 from comparisons of ice stability models and GRaND data (Prettyman et al., 2017). Our assumed density is 30% higher than the upper range of crustal densities determined from gravity and topography data (Ermakov et al., 2017).

The VIR spectra were fitted to a range of mineral end members by De Sanctis et al. (2015b). For the best fits, the minimum spectral mixing fraction for carbonates was 5% (calcite). For calcite, $\rho_{\text{mineral}} = 2.7$ g/cm^3 (Roberts et al., 1990) and the estimated concentration of calcite in Ceres regolith is 7.5 wt.%, which would contain about 1 wt.% carbon. The analysis by De Sanctis et al. (2015b) included magnetite as a possible neutral darkening agent. For the best fits, 60–80 vol.% magnetite was reported. Iron concentrations measured by GRaND constrain magnetite to be no more than 6 vol.% (McSween et al., 2017; Prettyman et al., 2017). Graphitized/amorphous carbon is a powerful darkening agent (Clark, 1983; De Sanctis et al., 2015b), and if present would allow larger mixing fractions for minerals with distinct absorption features such as carbonates. Thus, 1 wt.% could be regarded as a lower bound on C in carbonates on Ceres. This is far in excess of that generally found in CI and CM chondrites (0.08- to 0.55-wt.% reported by Alexander et al., 2015). For these meteorites, carbon is in the form of IOM, soluble organic matter (SOM), carbonates and an unidentified component, the latter typically making up less than half of the carbon inventory. Between IOM, SOM, and carbonates, most of the carbon is in IOM. The CI2 chondrite, Tagish Lake, is a notable exception, with higher concentrations of carbon than other carbonaceous chondrites. Tagish Lake has relatively high concentrations of carbonates (Brown et al., 2000; Grady et al., 2002), with around 1 wt.% C in carbonates estimated by Alexander et al. (2014).

Neutron measurements by GRaND permit high concentrations of C within Ceres' ice free regolith, greater than the 3.5 wt.% C found in CI chondrites (Lodders and Fegley, 1998; Prettyman et al., 2017). The difference between the Fe and H concentration within Ceres' regolith and that of the CI chondrites can be represented by the addition of carbon-rich material to the CI chondrite (nebular) composition. Three examples of dilution of a representative CI composition are illustrated in Fig. 8. Provided the added material does not contain Fe, the slopes of the dilution curves depend only on the mass fraction of hydrogen (f_H) in the added species.

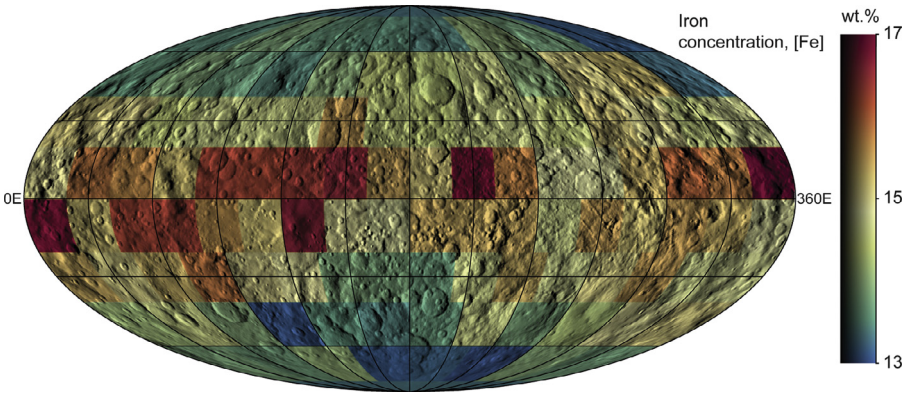

Fig. 7. Distribution of iron on Ceres measured by GRaND. The map data (color) were binned on 20-degree equal area pixels and superimposed on shaded relief for context.

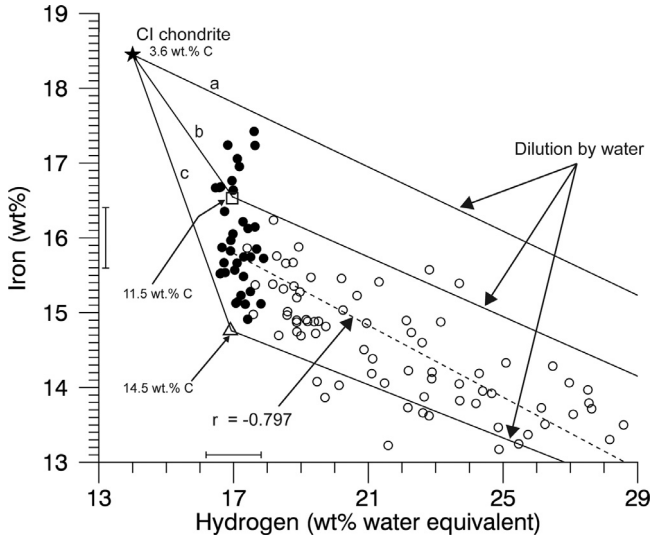

Fig. 8. Scatter plot of iron versus hydrogen measured by GRaND at Ceres. The data are from the global maps in Figs. 5A and 7. The global regression line (dashed) indicates a significant anti-correlation between Fe and H. Points equatorward of 20° latitude in the northern and southern hemisphere are filled (black). A representative CI chondrite (Orguiel) is shown (star): Hydrogen was determined via mass spectrometry (Alexander et al., 2012) and Fe was determined by x-ray fluorescence (Wolf and Palme, 2001). Lines drawn from the star show a) the effect of dilution by water (e.g. as ice or bound/adsorbed water molecules); b) the addition of 10 wt% IOM to the CI composition (open square); and c) the addition of 20 wt.% carbonaceous material (open triangle), modeled as a mixture of IOM and dolomite, to the CI composition. Water dilution trend lines are also shown for cases 'b' and 'c'. The models for IOM and carbonaceous material are described in the text. Error bars represent the uncertainty in individual data points. The error bar for the vertical axis gives the uncertainty in the iron concentration for individual pixels, which is dominated by the statistical uncertainty (Prettyman et al., 2017). The horizontal error bar gives the total analytical uncertainty in the hydrogen concentration for individual pixels, about 1 wt.%. The statistical contribution is small compared to the scatter in the equatorial data.

For example, in case 'a', variable amounts of water (H_2O, with $f_H = 11$ wt.%) are added directly to the CI chondrite composition. As discussed, the resulting dilution line does not intersect the data cloud. Thus, the addition of bound- or interlayer-water alone to CI cannot explain the data. Hydrogen must be in some other form, such as hydrated minerals or organic matter.

To illustrate the effect of added C, we modeled carbonaceous material as IOM, which we assumed to be a Murchison polymer containing CHON and with an H/C molar ratio of 0.71 and with $f_H = 4.8$ wt.% (Hayatsu & Anders, 1981; Derenne & Robert, 2010). When this material is added to the CI chondrite composition, the dilution trend intersects the data cloud (case 'b'). At the point from which the water dilution trend is drawn (open square in Fig. 8), the material contains 11.5 wt.% C.

We then modeled carbonaceous material as a mixture of IOM and carbonates in the form of dolomite. Case 'c' shows the dilution line for an IOM-carbonate mixture with a $C_{carbonate}/C_{IOM}$ ratio of 0.08, the average for CI chondrites reported by Alexander et al. (2015). The mixture has a H mass fraction of $f_H = 3.2$ wt.%. The dilution trend 'c' bounds the data cloud from below. The closest point to the equatorial data, from which the water dilution trend 'c' is drawn (open triangle in Fig. 8), has a total carbon concentration of 14.5 wt.%.

The equatorial data cloud can be modeled by varying the hydrogen content of IOM and the $C_{carbonate}/C_{IOM}$ mass ratio. The assumed compositional models for IOM and carbonates require high proportions of organic matter to carbonates in order to fit the equatorial Fe-H data. The data-cloud average is closely matched by a $C_{carbonate}/C_{IOM}$ ratio of 0.04, the minimum value for CI chondrites reported by Alexander et al. (2015).

Any model for the added materials would require $f_H = 4.6$ wt.% in order to match the equatorial average Fe-H data, assuming the added material contributes negligibly to iron content. Alternatives include salt hydrates, thought to be a component of crustal materials. Bright materials, which dot the surface of Ceres and are formed by hydrothermal activity or release of subsurface brine following impacts (e.g. Stein et al., 2017). These contain a mixture of Na-carbonates and phyllosilicates (e.g. illite or montmorillonite) and possibly ammonium carbonate [$(NH_4)_2CO_3$, $f_H = 8.4$ wt.%] (De Sanctis et al., 2016) and may be mixed with the global regolith in small quantities. Carrozzo et al. (2018) found evidence for hydrated Na-carbonate ($Na_2CO_3 \cdot H_2O$, $f_H = 1.6$ wt.%) in association with bright deposits, which could contribute to the global average hydrogen content. For Dawn's second extended mission, low altitude passes over the faculae in Occator crater are planned. This will enable improved elemental characterization of bright deposits and surrounding regions needed to better understand differences between Ceres' regolith and the CI chondrites.

The global Fe-H data set is consistent with modest variability in ice-free composition equatorward of 20° and dilution by water poleward of 20° (compare the regression line to water dilution trends in Fig. 8). Multiple lines of evidence and ice-stability considerations indicate that water ice is responsible for the observed dilution of Fe outside the equatorial region. Differences in the elemental composition of Ceres' non-icy regolith from that of CI chondrites result from ice-rock fractionation during Ceres evolution and/or compositional differences in accreted materials. Ceres' aqueously altered mineralogy suggests common origins with the carbonaceous chondrite parent bodies. These are thought to have formed outside the snow line, but within 5 AU of the sun, and

could have ingested comparable proportions of water and rock; although, it is conceivable that components of Ceres and the CI chondrites originated further out (De Sanctis et al., 2015b; McSween et al., 2017). If so, then differences in the abundances of H-, Fe-, and C-bearing species reflect low temperature, physical and chemical differentiation of Ceres' interior, which did not occur on the CI parent bodies. The presence of high concentrations of carbonaceous materials in combination with relatively low concentrations of Fe-bearing minerals may result from sedimentation of mud or oceanic materials during crustal formation, with heavier Fe-rich particles (magnetite and sulfides) settling at depth, producing a surface that is enriched in lighter elements (Prettyman et al., 2017).

4. Summary and conclusions

Smoothing of high-spatial-resolution data sets acquired by Dawn's optical instruments to the comparatively broad spatial resolution of GRaND is required for the joint analysis of surface elemental composition and mineralogy. To guarantee the most accurate comparisons, we use a physics-based smoothing algorithm that accounts for emission, transport, and detection of particles and the shape/topography of the target. The smoothing algorithm is applied to the same time-series of locations for which the data were acquired, and the same tools are used to map the smoothed counts as the data. This ensures that artifacts introduced by orbital sampling are the same in the elemental and smoothed mineral maps. The physics-based algorithm properly accounts for the mixing of irregular spatial features with varying size and contrast, enabling direct comparison of optical and nuclear data sets.

At Vesta, the distributions of OH and H are strikingly similar, despite the different depths sensed by VIR and GRaND (hundreds of μm and decimeters, respectively). This supports the hypothesis that hydrogen is primarily in the form of hydroxyl on Vesta. Hydroxyl is most likely in the form of phyllosilicates delivered by the infall of carbonaceous chondrite impactors following the emplacement of Vesta's eucritic crust. Small differences in the spatial patterns of OH and H imply that hydrogen is layered in some locations, albeit subtly. In Vesta's dark hemisphere (between 60E and 210E), hydrogen deposits are more extensive than hydroxyl, which indicates higher concentrations of hydrated minerals at depth.

At Ceres, the distributions of hydrogen by GRaND and hydrogen-bearing species (OH and NH_4^+) by VIR are dissimilar. At the spatial resolution of GRaND, the dynamic range of VIR absorption band depths is small compared that of hydrogen. The observed increase in hydrogen concentration with latitude is consistent with the presence of a global subsurface ice table, which on regional scales is at depths greater than sensed by VIR. Iron concentrations determined by GRaND follow a water-dilution trend when plotted as a function of regolith hydrogen content, consistent with the presence of subsurface water ice.

The VIR and GRaND data jointly constrain aspects of Ceres' surface chemistry and evolution. For example, GRaND Fe measurements place a firm upper bound on magnetite content, which supports graphitized carbon as an alternative to magnetite as a darkening agent. Minimum carbonate concentrations implied by VIR, together with carbonate/IOM ratios for carbonaceous chondrite meteorite analogs suggest high concentrations of carbon within Ceres' regolith. Organic matter, detected by VIR at Ernutet crater, might be widespread and may have been converted to carbon and graphite, e.g. via UV exposure, elsewhere on the surface. GRaND neutron measurements allow elevated carbon concentrations, equal to or in excess of that found in CI chondrites. Furthermore, added carbonaceous material can explain the difference between Fe and H concentrations measured by GRaND and the CI chondrites. If the CI chondrites are representative of the material from which Ceres accreted, then the elemental data indicate that ice and rock fractionated during Ceres' evolution producing a crust that differs in composition from the whole body. The observed difference between Ceres' regolith and the CI chondrites can be explained by sedimentation of mud and/or oceanic materials during crustal evolution, with heavier Fe-rich particles settling at depth, leaving the surface enriched in lighter elements.

Acknowledgements

This work was carried out under contract with the NASA Jet Propulsion Laboratory, which is operated by the California Institute of Technology in Pasadena, California. Partial support was provided by NASA's Solar System Exploration Research Virtual Institute's Toolbox for Research and Exploration (TREX) project. The Dawn mission is led by the University of California, Los Angeles under the auspices of the NASA Discovery Program. GRaND is operated by the Planetary Science Institute under contract with JPL. VIR is operated by the Italian National Institute for Astrophysics under contract with the Italian Space Agency. The VIR instrument was manufactured by Leonardo S.p.A. We thank reviewers Cristina De Sanctis and Tim Titus for their comments, which helped improve the manuscript. Data used in this study are available for download from the NASA Planetary Data System (https://pds-smallbodies.astro.umd.edu/data_sb/missions/dawn/).

Appendix

The 2.8 μm band-area map of Vesta (Fig. 3A) was determined using methods described by Ammannito et al. (2013) from data archived in the NASA Planetary Data System (PDS). The VIR visible and infrared reduced data records (Level 1B) were merged spectrally and spatially. The data were filtered to exclude spectra with an absolute reflectance lower that 0.001 for any wavelength between 0.7 and 2.5 μm. Finally, the spectra were smoothed to reduce noise (Fig. A1). The hydration band (HyB) was defined as the reflectance between 2.695 (HyB_start) and 3.405 (HyB_stop) μm. The continuum of the band was removed, dividing the spectrum by the straight line between HyB_start and HyB_stop. The intensity

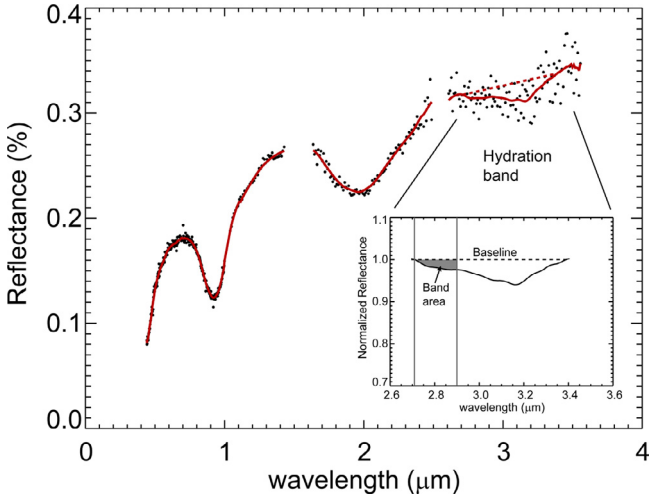

Fig. A1. Determination of the strength of the 2.8 μm hydroxyl absorption feature within the hydration band in reflectance spectra acquired at by VIR at Vesta. An example spectrum is shown (black points). The solid red lines show the result of the smoothing algorithm and the dotted line is the baseline of the hydration band. The inset shows the hydration band after normalization to the baseline. We used the area between the baseline and the normalized hydration band in the spectral range 2.7–2.9 μm as proxy for absorption by hydroxyl (shaded grey, inset).

of the hydration associated with the presence of hydroxyl was calculated as the area of the portion of the hydration band between 2.7 and 2.9 μm (Fig. A1, inset). The band area was computed and mapped for the Survey and High Altitude Mapping Orbit mission phases. Data from these mission phases were filtered for illumination conditions. Only spectra with incidence and emission angles lower than 70° and phase angles between 15° and 60° were mapped.

References

Alexander, C.M.O.'D., Bowden, R., Fogel, M.L., Howard, K.T., 2015. Carbonate abundances and isotopic compositions in chondrites. Meteorit. Planet. Sci. 50, 810–833. doi:10.1111/maps.12410.

Alexander, C.M.O.'D., Bowden, R., Fogel, M.L., Howard, K.T., Herd, C.D.K., Nittler, L.R., 2012. The provenances of asteroids, and their contributions to the volatile inventories of the terrestrial planets. Science 337, 721–723. doi:10.1126/science.1223474.

Alexander, C.M.O.'D., Howard, K.T., Bowden, R., Fogel, M.L., 2013. The classification of CM and CR chondrites using bulk H, C and N abundances and isotopic compositions. Geochim. Cosmochim. Acta 123, 244–260. doi:10.1016/j.gca.2013.05.019.

Alexander, C.M.O.D., Cody, G.D., Kebukawa, Y., Bowden, R., Fogel, M.L., Kilcoyne, A.L.D., Nittler, L.R., Herd, C.D.K., 2014. Elemental, isotopic, and structural changes in Tagish Lake insoluble organic matter produced by parent body processes. Meteorit. Planet. Sci. 49, 503–525. doi:10.1111/maps.12282.

Ammannito, E., De Sanctis, M.C., Combe, J.P., Frigeri, A., Jaumann, R., Longobardo, A., McSween, H.Y., Palomba, E., Tosi, F., Raymond, C.A., Russell, C.T., 2015. Compositional variations in the Vestan Rheasilvia basin. Icarus 259, 194–202. doi:10.1016/j.icarus.2015.05.017.

Ammannito, E., De Sanctis, M.C., Capaccioni, F., Teresa Capria, M., Carraro, F., Combe, J.-P., Fonte, S., Frigeri, A., Joy, S.P., Longobardo, A., Magni, G., Marchi, S., McCord, T.B., McFadden, L.A., McSween, H.Y., Palomba, E., Pieters, C.M., Polanskey, C.A., Raymond, C.A., Sunshine, J.M., Tosi, F., Zambon, F., Russell, C.T., 2013. Vestan lithologies mapped by the visual and infrared spectrometer on Dawn. Meteorit. Planet. Sci. 48, 2185–2198. doi:10.1111/maps.12192.

Ammannito, E., DeSanctis, M.C., Ciarniello, M., Frigeri, A., Carrozzo, F.G., Combe, J.-P., Ehlmann, B.L., Marchi, S., McSween, H.Y., Raponi, A., Toplis, M.J., Tosi, F., Castillo-Rogez, J.C., Capaccioni, F., Capria, M.T., Fonte, S., Giardino, M., Jaumann, R., Longobardo, A., Joy, S.P., Magni, G., McCord, T.B., McFadden, L.A., Palomba, E., Pieters, C.M., Polanskey, C.A., Rayman, M.D., Raymond, C.A., Schenk, P.M., Zambon, F., Russell, C.T., 2016. Distribution of phyllosilicates on the surface of Ceres. Science 353. doi:10.1126/science.aaf4279.

Bland, P.A., Travis, B.J., 2017. Giant convecting mud balls of the early solar system. Sci. Adv. 3. doi:10.1126/sciadv.1602514.

Bland, P.A., Jackson, M.D., Coker, R.F., Cohen, B.A., Webber, J.B.W., Lee, M.R., Duffy, C.M., Chater, R.J., Ardakani, M.G., McPhail, D.S., McComb, D.W., Benedix, G.K., 2009. Why aqueous alteration in asteroids was isochemical: High porosity≠high permeability. Earth Planet. Sci. Lett. 287, 559–568. doi:10.1016/j.epsl.2009.09.004.

Boynton, W., Feldman, W., Squyres, S., Prettyman, T., Brückner, J., Evans, L., Reedy, R., Starr, R., Arnold, J., Drake, D., 2002. Distribution of hydrogen in the near surface of Mars: Evidence for subsurface ice deposits. Science 297, 81–85. doi:10.1126/science.1073722.

Britt, D.T., Consolmagno, G.J.S.J., 2003. Stony meteorite porosities and densities: a review of data through 2001. Meteor. Planet. Sci. 38, 1161–1180. doi:10.1111/j.1945-5100.2003.tb00305.x.

Brown, P.G., Hildebrand, A.R., Zolensky, M.E., Grady, M., Clayton, R.N., Mayeda, T.K., Tagliaferri, E.L., Spalding, R., MacRae, N.D., Hoffman, E.L., Mittlefehdt, D.W., Wacker, J.F., Bird, J.A., Campbell, M.D., Carpenter, R., Gingerich, H., Glatiotis, M., Greiner, E., Mazur, M.J., McCausland, P.J., Plotkin, H., Mazur, T.R., 2000. The fall, recovery, orbit, and composition of the Tagish Lake meteorite: a new type of carbonaceous chondrite. Science 290, 320–325. doi:10.1126/science.290.5490.320.

Carrozzo, F.G., De Sanctis, M.C., Raponi, A., Ammannito, E., Castillo-Rogez, J., Ehlmann, B.L., Marchi, S., Stein, N., Ciarniello, M., Tosi, F., Capaccioni, F., Capria, M.T., Fonte, S., Formisano, M., Frigeri, A., Giardino, M., Longobardo, A., Magni, G., Palomba, E., Zambon, F., Raymond, C.A., Russell, C.T., 2018. Nature, formation, and distribution of carbonates on Ceres. Sci. Adv. 4. doi:10.1126/sciadv.1701645.

Cartwright, J.A., Ott, U., Mittlefehldt, D.W., 2014. The quest for regolithic howardites. Part 2: surface origins highlighted by noble gases. Geochim. Cosmochim. Acta 140, 488–508. doi:10.1016/j.gca.2014.05.033.

Cartwright, J.A., Ott, U., Mittlefehldt, D.W., Herrin, J.S., Herrmann, S., Mertzman, S.A., Mertzman, K.R., Peng, Z.X., Quinn, J.E., 2013. The quest for regolithic howardites. Part 1: two trends uncovered using noble gases. Geochim. Cosmochim. Acta 105, 395–421. doi:10.1016/j.gca.2012.11.047.

Castillo-Rogez, J.C., McCord, T.B., 2010. Ceres' evolution and present state constrained by shape data. Icarus 205, 443–459. doi:10.1016/j.icarus.2009.04.008.

Castillo-Rogez, J., Neveu, M., McSween, H., Fu, R., Toplis, M., Prettyman, T., Insights into Ceres' Evolution from Surface Composition, Meteorit. Planet. Sci., in review.

Clark, R.N., 1983. Spectral properties of mixtures of montmorillonite and dark carbon grains: implications for remote sensing minerals containing chemically and physically adsorbed water. J. Geophys. Res.: Solid Earth 88, 10635–10644. doi:10.1029/JB088iB12p10635.

Combe, J.-P., Raponi, A., Tosi, F., De Sanctis, M.C., Carrozzo, F.G., Zambon, F., Ammannito, E., Hughson, K.H.G., Nathues, A., Hoffmann, M., Platz, T., Thangjam, G., Schorghofer, N., Schröder, S., Byrne, S., Landis, M.E., Ruesch, O., McCord, T.B., Johnson, K.E., Singh, S.M., Raymond, C.A., Russell, C.T., 2017. Exposed H2O-rich areas detected on Ceres with the dawn visible and infrared mapping spectrometer. Icarus doi:10.1016/j.icarus.2017.12.008.

Combe, J.P., McCord, T.B., Tosi, F., Ammannito, E., Carrozzo, F.G., De Sanctis M.C., RaponiA., Byrne, S., Landis, M.E., Hughson, K.H., Raymond, C.A., Russell, C.T., 2016. Detection of local H_2O exposed at the surface of Ceres. Science 353, aaf3010. doi:10.1126/science.aaf3010.

De Sanctis, M.C., Combe, J.P., Ammannito, A., Frigeri, A., Longobardo, A., Palomba, E., Tosi, F., Zambon, F., Stephan, K., Raymond, C.A., Russell, C.T., 2015a. Eucritic crust remnants and the effect of in-falling hydrous carbonaceous chondrites characterizing the composition of Vesta's Marcia region. Icarus 259, 91–115. doi:10.1016/j.icarus.2015.05.014.

De Sanctis, M.C., Coradini, A., Ammannito, E., Filacchione, G., Capria, M.T., Fonte, S., Magni, G., Barbis, A., Bini, A., Dami, M., Ficai-Veltroni, I., Preti, G., 2011. The VIR spectrometer. Space Sci. Rev. 163, 329–369. doi:10.1007/s11214-010-9668-5.

De Sanctis, M.C., Combe, J.P., Ammannito, E., Palomba, E., Longobardo, A., McCord, T.B., Marchi, S., Capaccioni, F., Capria, M.T., Mittlefehldt, D.W., Pieters, C.M., Sunshine, J., Tosi, F., Zambon, F., Carraro, F., Fonte, S., Frigeri, A., Magni, G., Raymond, C.A., Russell, C.T., Turrini, D., 2012a. Detection of widespread hydrated materials on Vesta by the VIR imaging spectrometer on board the Dawn mission. Astrophys. J. 758, L36. doi:10.1088/2041-8205/758/2/l36.

De Sanctis, M.C., Ammannito, E., McSween, H.Y., Raponi, A., Marchi, S., Capaccioni, F., Capria, M.T., Carrozzo, F.G., Ciarniello, M., Fonte, S., Formisano, M., Frigeri, A., Giardino, M., Longobardo, A., Magni, G., McFadden, L.A., Palomba, E., Pieters, C.M., Tosi, F., Zambon, F., Raymond, C.A., Russell, C.T., 2017. Localized aliphatic organic material on the surface of Ceres. Science 355, 719–722. doi:10.1126/science.aaj2305.

De Sanctis, M.C., Ammannito, E., Capria, M.T., Tosi, F., Capaccioni, F., Zambon, F., Carraro, F., Fonte, S., Frigeri, A., Jaumann, R., Magni, G., Marchi, S., McCord, T.B., McFadden, L.A., McSween, H.Y., Mittlefehldt, D.W., Nathues, A., Palomba, E., Pieters, C.M., Raymond, C.A., Russell, C.T., Toplis, M.J., Turrini, D., 2012b. Spectroscopic characterization of mineralogy and its diversity across Vesta. Science 336, 697–700. doi:10.1126/science.1219270.

De Sanctis, M.C., Raponi, A., Ammannito, E., Ciarniello, M., Toplis, M.J., McSween, H.Y., Castillo-Rogez, J.C., Ehlmann, B.L., Carrozzo, F.G., Marchi, S., Tosi, F., Zambon, F., Capaccioni, F., Capria, M.T., Fonte, S., Formisano, M., Frigeri, A., Giardino, M., Longobardo, A., Magni, G., Palomba, E., McFadden, L.A., Pieters, C.M., Jaumann, R., Schenk, P., Mugnuolo, R., Raymond, C.A., Russell, C.T., 2016. Bright carbonate deposits as evidence of aqueous alteration on (1) Ceres. Nature 536, 54–57. doi:10.1038/nature18290.

De Sanctis, M.C., Ammannito, E., Raponi, A., Marchi, S., McCord, T.B., McSween, H.Y., Capaccioni, F., Capria, M.T., Carrozzo, F.G., Ciarniello, M., Longobardo, A., Tosi, F., Fonte, S., Formisano, M., Frigeri, A., Giardino, M., Magni, G., Palomba, E., Turrini, D., Zambon, F., Combe, J.P., Feldman, W., Jaumann, R., McFadden, L.A., Pieters, C.M., Prettyman, T., Toplis, M., Raymond, C.A., Russell, C.T., 2015b. Ammoniated phyllosilicates with a likely outer Solar System origin on (1) Ceres. Nature 528, 241–244. doi:10.1038/nature16172.

Derenne, S., Robert, F., 2010. Model of molecular structure of the insoluble organic matter isolated from Murchison meteorite. Meteorit. Planet. Sci. 45, 1461–1475. doi:10.1111/j.1945-5100.2010.01122.x.

Eke, V.R., Bower, K.E., Diserens, S., Ryder, M., Yeomans, P.E.L., Teodoro, L.F.A., Elphic, R.C., Feldman, W.C., Hermalyn, B., Lavelle, C.M., Lawrence, D.J., 2015. The effect of craters on the lunar neutron flux. J. Geophys. Res.: Planets 120, 1377–1395. doi:10.1002/2015JE004856.

Ermakov, A.I., Fu, R.R., Castillo-Rogez, J.C., Raymond, C.A., Park, R.S., Preusker, F., Russell, C.T., Smith, D.E., Zuber, M.T., 2017. Constraints on Ceres' internal structure and evolution from its shape and gravity measured by the Dawn Spacecraft. J. Geophys. Res.: Planets 122, 2267–2293. doi:10.1002/2017JE005302.

Fanale, F.P., Salvail, J.R., 1989. The water regime of asteroid (1) Ceres. Icarus 82, 97–110.

Formisano, M., De Sanctis, M.C., Magni, G., Federico, C., Capria, M.T., 2016. Ceres water regime: surface temperature, water sublimation and transient exo(atmo)sphere. Mon. Not. R. Astron. Soc. 455, 1892–1904. doi:10.1093/mnras/stv2344.

Fu, R.R., Ermakov, A.I., Marchi, S., Castillo-Rogez, J.C., Raymond, C.A., Hager, B.H., Zuber, M.T., King, S.D., Bland, M.T., Cristina De Sanctis, M., Preusker, F., Park, R.S., Russell, C.T., 2017. The interior structure of Ceres as revealed by surface topography. Earth Planet. Sci. Lett. 476, 153–164. doi:10.1016/j.epsl.2017.07.053.

Fyfe, W.S., 1974. Heats of chemical reactions and submarine heat production. Geophys. J. R. Astron. Soc. 37, 213–215. doi:10.1111/j.1365-246X.1974.tb02454.x.

Gaskell, R.W., Barnouin-Jha, O.S., Scheeres, D.J., Konopliv, A.S., Mukai, T., Abe, S., Saito, J., Ishiguro, M., Kubota, T., Hashimoto, T., Kawaguchi, J., Yoshikawa, M., Shirakawa, K., Kominato, T., Hirata, N., Demura, H., 2008. Characterizing and navigating small bodies with imaging data. Meteorit. Planet. Sci. 43, 1049–1061. doi:10.1111/j.1945-5100.2008.tb00692.x.

Gasnault, O., Maurice, S., Lawrence, D.J., 2003. Low resolution planetary experiments: gridding and mapping routines using IDL. In: ISPRS Workshop: Advances in Planetary Mapping, International Society for Photogrammetry and Remote Sensing, Houston, TX.

Grady, M.M., Verchovsky, A.B., Franchi, I.A., Wright, I.P., Pillinger, C.T., 2002. Light element geochemistry of the Tagish Lake CI2 chondrite: comparison with CI1

and CM2 meteorites. Meteor. Planet. Sci. 37, 713–735. doi:10.1111/j.1945-5100.2002.tb00851.x.
Haines, E.L., Etchegaray-Ramirez, M.I., Metzger, A.E., 1978. Thorium concentrations in the lunar surface. II: deconvolution modeling and its application to the regions of Aristarchus and Mare Smythii. Proc. Lunar Planet. Sci. Conf. 9th 2985–3013.
Hans, U., Kleine, T., Bourdon, B., 2013. Rb–Sr chronology of volatile depletion in differentiated protoplanets: BABI, ADOR and ALL revisited. Earth Planet. Sci. Lett. 374, 204–214. doi:10.1016/j.epsl.2013.05.029.
Hapke, B., 1981. Bidirectional reflectance spectroscopy: 1. Theory. J. Geophys. Res.: Solid Earth 86, 3039–3054. doi:10.1029/JB086iB04p03039.
Hayatsu, R., Anders, E., 1981. Organic compounds in meteorites and their origins. In: Cosmo- and Geochemistry. Topics in Current Chemistry, vol 99. Springer, Berlin, Heidelberg, pp. 1–37. doi:10.1007/3-540-10920-X_13.
Hayne, P.O., Aharonson, O., 2015. Thermal stability of ice on Ceres with rough topography. J. Geophys. Res.: Planets 120, 1567–1584. doi:10.1002/2015je004887.
Hendrix, A.R., Vilas, F., Li, J.-Y., 2016. The UV signature of carbon in the solar system. Meteorit. Planet. Sci. 51, 105–115. doi:10.1111/maps.12575.
Howard, K.T., Alexander, C.M.O.D., Schrader, D.L., Dyl, K.A., 2015. Classification of hydrous meteorites (CR, CM and C2 ungrouped) by phyllosilicate fraction: PSD-XRD modal mineralogy and planetesimal environments. Geochim. Cosmochim. Acta 149, 206–222. doi:10.1016/j.gca.2014.10.025.
Jaumann, R., Nass, A., Otto, K., Krohn, K., Stephan, K., McCord, T.B., Williams, D.A., Raymond, C.A., Blewett, D.T., Hiesinger, H., Yingst, R.A., De Sanctis, M.C., Palomba, E., Roatsch, T., Matz, K.D., Preusker, F., Scholten, F., Russell, C.T., 2014. The geological nature of dark material on Vesta and implications for the subsurface structure. Icarus 240, 3–19. doi:10.1016/j.icarus.2014.04.035.
Jaumann, R., Williams, D.A., Buczkowski, D.L., Yingst, R.A., Preusker, F., Hiesinger, H., Schmedemann, N., Kneissl, T., Vincent, J.B., Blewett, D.T., Buratti, B.J., Carsenty, U., Denevi, B.W., De Sanctis M.C., GarryW.B., Keller, H.U., Kersten, E., Krohn, K., Li, J.-Y., Marchi, S., Matz, K.D., McCord, T.B., McSween, H.Y., Mest, S.C., Mittlefehldt, D.W., Mottola, S., Nathues, A., Neukum, G., O'Brien, D.P., Pieters, C.M., Prettyman, T.H., Raymond, C.A., Roatsch, T., Russell, C.T., Schenk, P., Schmidt, B.E., Scholten, F., Stephan, K., Sykes, M.V., Tricarico, P., Wagner, R., Zuber, M.T., Sierks, H., 2012. Vesta's shape and morphology. Science 336, 687–690. doi:10.1126/science.1219122.
Kaplan, H.H., Milliken, R.E., O'D. Alexander, C.M., 2018. New constraints on the abundance and composition of organic matter on ceres. Geophys. Res. Lett., p. 45, Abstract #1155. doi:10.1029/2018GL077913.
King, T.V.V., Clark, R.N., Calvin, W.M., Sherman, D.M., Brown, R.H., 1992. Evidence for ammonium-bearing minerals on Ceres. Science 255, 1551–1553. doi:10.1126/science.255.5051.1551.
Kuppers, M., O'Rourke, L., Bockelee-Morvan, D., Zakharov, V., Lee, S., von Allmen, P., Carry, B., Teyssier, D., Marston, A., Muller, T., Crovisier, J., Barucci, M.A., Moreno, R., 2014. Localized sources of water vapour on the dwarf planet (1) Ceres. Nature 505, 525–527. doi:10.1038/nature12918.
Landis, M.E., Byrne, S., Schörghofer, N., Schmidt, B.E., Hayne, P.O., Castillo-Rogez, J., Sykes, M.V., Combe, J.P., Ermakov, A.I., Prettyman, T.H., Raymond, C.A., Russell, C.T., 2017. Conditions for sublimating water ice to supply Ceres' exosphere. J. Geophys. Res.: Planets 122, 1984–1995. doi:10.1002/2017JE005335.
Lawrence, D.J., Elphic, R.C., Feldman, W.C., Prettyman, T.H., Gasnault, O., Maurice, S., 2003. Small-area thorium features on the lunar surface. J. Geophys. Res.: Planets 108. doi:10.1029/2003JE002050.
Lawrence, D.J., Feldman, W.C., Elphic, R.C., Hagerty, J.J., Maurice, S., McKinney, G.W., Prettyman, T.H., 2006. Improved modeling of Lunar Prospector neutron spectrometer data: Implications for hydrogen deposits at the lunar poles. J. Geophys. Res. 111. doi:10.1029/2005je002637.
Lawrence, D.J., Peplowski, P.N., Prettyman, T.H., Feldman, W.C., Bazell, D., Mittlefehldt, D.W., Reedy, R.C., Yamashita, N., 2013. Constraints on Vesta's elemental composition: fast neutron measurements by Dawn's gamma ray and neutron detector. Meteorit. Planet. Sci. 48, 2271–2288. doi:10.1111/maps.12187.
Lebofsky, L.A., Feierberg, M.A., Tokunaga, A.T., Larson, H.P., Johnson, J.R., 1981. The 1.7- to 4.2-μm spectrum of asteroid 1 Ceres: evidence for structural water in clay minerals. Icarus 48, 453–459. doi:10.1016/0019-1035(81)90055-5.
Lodders K. (2010) Solar system abundances of the elements. In: Goswami A., Reddy B. (eds) Principles and Perspectives in Cosmochemistry. Astrophysics and Space Science Proceedings. Springer, Berlin, Heidelberg, doi: 10.1007/978-3-642-10352-0_8
Lodders, K., Fegley Jr., B., 1998. The Planetary Scientist's Companion. Oxford University Press ISBN-10: 0195116941.
Lunning, N.G., Welten, K.C., McSween, H.Y., Caffee, M.W., Beck, A.W., 2016. Grosvenor Mountains 95 howardite pairing group: Insights into the surface regolith of asteroid 4 Vesta. Meteorit. Planet. Sci. 51, 167–194. doi:10.1111/maps.12580.
Mandler, B.E., Elkins-Tanton, L.T., 2013. The origin of eucrites, diogenites, and olivine diogenites: Magma ocean crystallization and shallow magma chamber processes on Vesta. Meteorit. Planet. Sci. 48, 2333–2349. doi:10.1111/maps.12135.
Marchi, S., Bottke, W.F., Cohen, B.A., Wünnemann, K., Kring, D.A., McSween, H.Y., De Sanctis, M.C., O'Brien, D.P., Schenk, P., Raymond, C.A., Russell, C.T., 2013. High-velocity collisions from the lunar cataclysm recorded in asteroidal meteorites. Nat. Geosci. 6, 303–307. doi:10.1038/ngeo1769.
Marchi, S., McSween, H.Y., O'Brien, D.P., Schenk, P., De Sanctis, M.C., Gaskell, R., Jaumann, R., Mottola, S., Preusker, F., Raymond, C.A., Roatsch, T., Russell, C.T., 2012. The violent collisional history of asteroid 4 Vesta. Science 336, 690–694. doi:10.1126/science.1218757.
Marchi, S., Ermakov, A.I., Raymond, C.A., Fu, R.R., O'Brien, D.P., Bland, M.T., Ammannito, E., De Sanctis, M.C., Bowling, T., Schenk, P., Scully, J.E.C., Buczkowski, D.L., Williams, D.A., Hiesinger, H., Russell, C.T., 2016. The missing large impact craters on Ceres. Nature Commun. 7, 12257. doi:10.1038/ncomms12257.
McCord, T.B., Sotin, C., 2005. Ceres: evolution and current state. J. Geophys. Res. 110, E05009. doi:10.1029/2004je002244.
McCord, T.B., Li, J.Y., Combe, J.P., McSween, H.Y., Jaumann, R., Reddy, V., Tosi, F., Williams, D.A., Blewett, D.T., Turrini, D., Palomba, E., Pieters, C.M., De Sanctis, M.C., Ammannito, E., Capria, M.T., Le Corre, L., Longobardo, A., Nathues, A., Mittlefehldt, D.W., Schröder, S.E., Hiesinger, H., Beck, A.W., Capaccioni, F., Carsenty, U., Keller, H.U., Denevi, B.W., Sunshine, J.M., Raymond, C.A., Russell, C.T., 2012. Dark material on Vesta from the infall of carbonaceous volatile-rich material. Nature 491, 83–86. doi:10.1038/nature11561.
McKinney, G.W., Lawrence, D.J., Prettyman, T.H., Elphic, R.C., Feldman, W.C., Hagerty, J.J., 2006. MCNPX benchmark for cosmic ray interactions with the Moon. J. Geophys. Res. 111, E06004. doi:10.1029/2005JE002551.
McSween, H.Y., Mittlefehldt, D.W., Beck, A.W., Mayne, R.G., McCoy, T.J., 2011. HED meteorites and their relationship to the geology of Vesta and the Dawn Mission. Space Sci. Rev. 163, 141–174. doi:10.1007/s11214-010-9637-z.
McSween, H.Y., Emery, J.P., Rivkin, A.S., Toplis, M.J., C. Castillo-Rogez, J., Prettyman, T.H., De Sanctis, M.C., Pieters, C.M., Raymond, C.A., Russell, C.T., 2017. Carbonaceous chondrites as analogs for the composition and alteration of Ceres. Meteorit. Planet. Sci. doi:10.1111/maps.12947.
McSween, H.Y., Binzel, R.P., De Sanctis, M.C., Ammannito, E., Prettyman, T.H., Beck, A.W., Reddy, V., Le Corre, L., Gaffey, M.J., McCord, T.B., Raymond, C.A., Russell, C.T., 2013. Dawn; the Vesta-HED connection; and the geologic context for eucrites, diogenites, and howardites. Meteorit. Planet. Sci. 48, 2090–2104. doi:10.1111/maps.12108.
Mittlefehldt, D.W., 2015. Asteroid (4) Vesta: I. The howardite-eucrite-diogenite (HED) clan of meteorites. Chem. Erde 75, 155–183. doi:10.1016/j.chemer.2014.08.002.
Nathues, A., Hoffmann, M., Cloutis, E.A., Schäfer, M., Reddy, V., Christensen, U., Sierks, H., Thangjam, G.S., Le Corre, L., Mengel, K., Vincent, J.-B., Russell, C.T., Prettyman, T., Schmedemann, N., Kneissl, T., Raymond, C., Gutierrez-Marques, P., Hall, I., Büttner, I., 2014. Detection of serpentine in exogenic carbonaceous chondrite material on Vesta from Dawn FC data. Icarus 239, 222–237. doi:10.1016/j.icarus.2014.06.003.
Neveu, M., Desch, S.J., 2015. Geochemistry, thermal evolution, and cryovolcanism on Ceres with a muddy ice mantle. Geophys. Res. Lett. 42, 10,197–10,206. doi:10.1002/2015gl066375.
O'Brien, D.P., Marchi, S., Morbidelli, A., Bottke, W.F., Schenk, P.M., Russell, C.T., Raymond, C.A., 2014. Constraining the cratering chronology of Vesta. Planet. Space Sci. 103, 131–142. doi:10.1016/j.pss.2014.05.013.
Palomba, E., Longobardo, A., De Sanctis, M.C., Zambon, F., Tosi, F., Ammannito, E., Capaccioni, F., Frigeri, A., Capria, M.T., Cloutis, E.A., Jaumann, R., Combe, J.-P., Raymond, C.A., Russell, C.T., 2014. Composition and mineralogy of dark material units on Vesta. Icarus 240, 58–72. doi:10.1016/j.icarus.2014.04.040.
Peplowski, P.N., Lawrence, D.J., Prettyman, T.H., Yamashita, N., Bazell, D., Feldman, W.C., Le Corre, L., McCoy, T.J., Reddy, V., Reedy, R.C., Russell, C.T., Toplis, M.J., 2013. Compositional variability on the surface of 4 Vesta revealed through GRaND measurements of high-energy gamma rays. Meteorit. Planet. Sci. 48, 2252–2270. doi:10.1111/maps.12176.
Pieters, C.M., McFadden, L.A., Prettyman, T., De Sanctis, M.C., McCord, T.B., Hiroi, T., Klima, R., Li, J.-Y., Jaumann, R., 2011. Surface composition of Vesta: issues and integrated approach. Space Sci. Rev. 163, 117–139. doi:10.1007/s11214-011-9809-5.
Pieters, C.M., Nathues, A., Thangjam, G., Hoffmann, M., Platz, T., Sanctis, M.C.d., Ammannito, E., Tosi, F., Zambon, F., Pasckert, J.H., Hiesinger, H., Schröder, S.E., Jaumann, R., Matz, K.D., Castillo-Rogez, J.C., Ruesch, O., McFadden, L.A., O'Brien, D.P., Sykes, M., Raymond, C.A., Russell, C.T., 2017. Geologic constraints on the origin of red organic-rich material on Ceres. Meteorit. Planet. Sci. doi:10.1111/maps.13008.
Pizzarello, S., Huang, Y., Becker, L., Poreda, R.J., Nieman, R.A., Cooper, G., Williams, M., 2001. The organic content of the Tagish Lake meteorite. Science 293, 2236–2239. doi:10.1126/science.1062614.
Prettyman, T.H., Feldman, W.C., Mellon, M.T., McKinney, G.W., Boynton, W.V., Karunatillake, S., Lawrence, D.J., Maurice, S., Metzger, A.E., Murphy, J.R., Squyres, S.W., Starr, R.D., Tokar, R.L., 2004. Composition and structure of the Martian surface at high southern latitudes from neutron spectroscopy. J. Geophys. Res. 109. doi:10.1029/2003JE002139.
Prettyman, T.H., 2014. Remote sensing of chemical elements using nuclear spectroscopy. In: Spohn, T., Johnson, T., Breuer, D. (Eds.), Encyclopedia of the Solar System (Third Edition). Elsevier, pp. 1161–1183. ISBN-10: 0124158455.
Prettyman, T.H., 2017. Dawn GRaND Ephemeris, Pointing, and Geometry, V3. DAWN-A-GRAND-3-RDR-CERES-COUNTS-V1.0,. NASA Planetary Data System https://pds.jpl.nasa.gov.
Prettyman, T.H., Hendricks, J.S., 2015. Nuclear spectroscopy of irregular bodies: comparison of Vesta and Phobos. 46th Lunar and Planetary Science Conferences, 16-20 March, The Woodlands, TX, Abstract #1832 https://www.hou.usra.edu/meetings/lpsc2015/pdf/1501.pdf.
Prettyman, T.H., Feldman, W.C., Titus, T.N., 2009. Characterization of Mars' seasonal caps using neutron spectroscopy. J. Geophys. Res. 114. doi:10.1029/2008je003275.
Prettyman, T.H., Hagerty, J.J., Elphic, R.C., Feldman, W.C., Lawrence, D.J., McKinney, G.W., Vaniman, D.T., 2006. Elemental composition of the lunar surface: analysis of gamma ray spectroscopy data from Lunar Prospector. J. Geophys. Res. 111, E12007. doi:10.1029/2005je002656.
Prettyman, T.H., Yamashita, N., Reedy, R.C., McSween, H.Y., Mittlefehldt, D.W., Hen-

dricks, J.S., Toplis, M.J., 2015. Concentrations of potassium and thorium within Vesta's regolith. Icarus 259, 39–52. doi:10.1016/j.icarus.2015.05.035.
Prettyman, T.H., Feldman, W.C., McSween Jr., H.Y., Dingler, R.D., Enemark, D.C., Patrick, D.E., Storms, S.A., Hendricks, J.S., Morgenthaler, J.P., Pitman, K.M., Reedy, R.C., 2011. Dawn's gamma ray and neutron detector. Space Sci. Rev. 163, 371–459. doi:10.1007/s11214-011-9862-0.
Prettyman, T.H., Mittlefehldt, D.W., Yamashita, N., Beck, A.W., Feldman, W.C., Hendricks, J.S., Lawrence, D.J., McCoy, T.J., McSween, H.Y., Peplowski, P.N., Reedy, R.C., Toplis, M.J., Le Corre, L., Mizzon, H., Reddy, V., Titus, T.N., Raymond, C.A., Russell, C.T., 2013. Neutron absorption constraints on the composition of 4 Vesta. Meteorit. Planet. Sci. 48, 2211–2236. doi:10.1111/maps.12244.
Prettyman, T.H., Yamashita, N., Toplis, M.J., McSween, H.Y., Schorghofer, N., Marchi, S., Feldman, W.C., Castillo-Rogez, J., Forni, O., Lawrence, D.J., Ammannito, E., Ehlmann, B.L., Sizemore, H.G., Joy, S.P., Polanskey, C.A., Rayman, M.D., Raymond, C.A., Russell, C.T., 2017. Extensive water ice within Ceres' aqueously altered regolith: evidence from nuclear spectroscopy. Science 355, 55–59. doi:10.1126/science.aah6765.
Prettyman, T.H., Mittlefehldt, D.W., Yamashita, N., Lawrence, D.J., Beck, A.W., Feldman, W.C., McCoy, T.J., McSween, H.Y., Toplis, M.J., Titus, T.N., Tricarico, P., Reedy, R.C., Hendricks, J.S., Forni, O., Le Corre L., LiJ.Y., Mizzon, H., Reddy, V., Raymond, C.A., Russell, C.T., 2012. Elemental mapping by Dawn reveals exogenic H in Vesta's regolith. Science 338, 242–246. doi:10.1126/science.1225354.
Raponi, A., De Sanctis, M.C., Frigeri, A., Ammannito, E., Ciarniello, M., Formisano, M., Combe, J.-P., Magni, G., Tosi, F., Carrozzo, F.G., Fonte, S., Giardino, M., Joy, S.P., Polanskey, C.A., Rayman, M.D., Capaccioni, F., Capria, M.T., Longobardo, A., Palomba, E., Zambon, F., Raymond, C.A., Russell, C.T., 2018. Variations in the amount of water ice on Ceres' surface suggest a seasonal water cycle. Sci. Adv. 4. doi:10.1126/sciadv.aao3757.
Reddy, V., Le Corre, L., O'Brien, D.P., Nathues, A., Cloutis, E.A., Durda, D.D., Bottke, W.F., Bhatt, M.U., Nesvorny, D., Buczkowski, D., Scully, J.E.C., Palmer, E.M., Sierks, H., Mann, P.J., Becker, K.J., Beck, A.W., Mittlefehldt, D., Li, J.-Y., Gaskell, R., Russell, C.T., Gaffey, M.J., McSween, H.Y., McCord, T.B., Combe, J.-P., Blewett, D., 2012. Delivery of dark material to Vesta via carbonaceous chondritic impacts. Icarus 221, 544–559. doi:10.1016/j.icarus.2012.08.011.
Righter, K., Drake, M.J., 1997. A magma ocean on Vesta: core formation and petrogenesis of eucrites and diogenites. Meteorit. Planet. Sci. 32, 929–944. doi:10.1111/j.1945-5100.1997.tb01582.x.
Rivkin, A.S., Li, J.-Y., Milliken, R.E., Lim, L.F., Lovell, A.J., Schmidt, B.E., McFadden, L.A., Cohen, B.A., 2010. The surface composition of Ceres. Space Sci. Rev. 163, 95–116. doi:10.1007/s11214-010-9677-4.
Roatsch, T., Kersten, E., Matz, K.D., Preusker, F., Scholten, F., Jaumann, R., Raymond, C.A., Russell, C.T., 2016. Ceres survey atlas derived from Dawn Framing Camera images. Planet. Space Sci. 121, 115–120. doi:10.1016/j.pss.2015.12.005.
Roberts, W.L., Campbell, T.J., Rapp, G.R., 1990. Encyclopedia of Minerals. Van Nostrand Reinhold ISBN-10: 0442276818.
Russell, C.T., Coradini, A., Christensen, U., De Sanctis, M.C., Feldman, W.C., Jaumann, R., Keller, H.U., Konopliv, A.S., McCord, T.B., McFadden, L.A., McSween, H.Y., Mottola, S., Neukum, G., Pieters, C.M., Prettyman, T.H., Raymond, C.A., Smith, D.E., Sykes, M.V., Williams, B.G., Wise, J., Zuber, M.T., 2004. Dawn: a journey in space and time. Planet. Space Sci. 52, 465–489. doi:10.1016/j.pss.2003.06.013.
Russell, C.T., Raymond, C.A., Coradini, A., McSween, H.Y., Zuber, M.T., Nathues, A., De Sanctis, M.C., Jaumann, R., Konopliv, A.S., Preusker, F., Asmar, S.W., Park, R.S., Gaskell, R., Keller, H.U., Mottola, S., Roatsch, T., Scully, J.E.C., Smith, D.E., Tricarico, P., Toplis, M.J., Christensen, U.R., Feldman, W.C., Lawrence, D.J., McCoy, T.J., Prettyman, T.H., Reedy, R.C., Sykes, M.E., Titus, T.N., 2012. Dawn at Vesta: testing the protoplanetary paradigm. Science 336, 684–686. doi:10.1126/science.1219381.
Russell, C.T., Raymond, C.a., Ammannito, E., Buczkowski, D.L., De Sanctis, M.C., Hiesinger, H., Jaumann, R., Konopliv, A.S., McSween, H.Y., Nathues, A., Park, R.S., Pieters, C.M., Prettyman, T.H., McCord, T.B., McFadden, L.A., Mottola, S., Zuber, M.T., Joy, S.P., Polanskey, C.A., Rayman, M.D., Castillo-Rogez, J.C., Chi, P.J., Combe, J.P., Ermakov, A.I., Fu, R.R., Hoffmann, M., Jia, Y.D., King, S.D., Lawrence, D.J., Li, J.-Y., Marchi, S., Preusker, F., Roatsch, T., Ruesch, O., Schenk, P., Villarreal, M.N., Yamashita, N., 2016. Dawn arrives at Ceres: exploration of a small, volatile-rich world. Science 353, 1008–1010. doi:10.1126/science.aaf4219.
Sato, K., Miyamoto, M., Zolensky, M.E., 1997. Absorption bands near three micrometers in diffuse reflectance spectra of carbonaceous chondrites: comparison with asteroids. Meteorit. Planet. Sci. 32, 503–507. doi:10.1111/j.1945-5100.1997.tb01295.x.
Schenk, P., O'Brien, D.P., Marchi, S., Gaskell, R., Preusker, F., Roatsch, T., Jaumann, R., Buczkowski, D., McCord, T., McSween, H.Y., Williams, D., Yingst, A., Raymond, C., Russell, C., 2012. The geologically recent giant impact basins at Vesta's South Pole. Science 336, 694–697. doi:10.1126/science.1223272.
Schmedemann, N., Kneissl, T., Ivanov, B.A., Michael, G.G., Wagner, R.J., Neukum, G., Ruesch, O., Hiesinger, H., Krohn, K., Roatsch, T., Preusker, F., Sierks, H., Jaumann, R., Reddy, V., Nathues, A., Walter, S.H.G., Neesemann, A., Raymond, C.A., Russell, C.T., 2014. The cratering record, chronology and surface ages of (4) Vesta in comparison to smaller asteroids and the ages of HED meteorites. Planet. Space Sci. 103, 104–130. doi:10.1016/j.pss.2014.04.004.
Schmidt, B.E., Hughson, K.H.G., Chilton, H.T., Scully, J.E.C., Platz, T., Nathues, A., Sizemore, H., Bland, M.T., Byrne, S., Marchi, S., O'Brien David, P., Schorghofer, N., Hiesinger, H., Jaumann, R., Pasckert, J.H., Lawrence, J.D., Buzckowski, D., Castillo-Rogez, J.C., Sykes, M.V., Schenk, P.M., DeSanctis, M.-C., Mitri, G., Formisano, M., Li, J.-Y., Reddy, V., LeCorre, L., Russell, C.T., Raymond, C.A., 2017. Geomorphological evidence for ground ice on dwarf planet Ceres. Nat. Geosci. 10, 338–343. doi:10.1038/ngeo2936.
Schorghofer, N., 2016. Predictions of depth-to-ice on asteroids based on an asynchronous model of temperature, impact stirring, and ice loss. Icarus 276, 88–95. doi:10.1016/j.icarus.2016.04.037.
Schorghofer, N., Byrne, S., Landis, M.E., Mazarico, E., Prettyman, T.H., Schmidt, B.E., Villarreal, M.N., Castillo-Rogez, J., Raymond, C.A., Russell, C.T., 2017. The putative cerean exosphere. Astrophys. J. 850, 85. doi:10.3847/1538-4357/aa932f.
Scully, J.E.C., Russell, C.T., Yin, A., Jaumann, R., Carey, E., Castillo-Rogez, J., McSween, H.Y., Raymond, C.A., Reddy, V., Le Corre, L., 2015. Geomorphological evidence for transient water flow on Vesta. Earth Planet. Sci. Lett. 411, 151–163. doi:10.1016/j.epsl.2014.12.004.
Sierks, H., Keller, H.U., Jaumann, R., Michalik, H., Behnke, T., Bubenhagen, F., Büttner, I., Carsenty, U., Christensen, U., Enge, R., Fiethe, B., Gutiérrez Marqués, P., Hartwig, H., Krüger, H., Kühne, W., Maue, T., Mottola, S., Nathues, A., Reiche, K.U., Richards, M.L., Roatsch, T., Schröder, S.E., Szemerey, I., Tschentscher, M., 2011. The Dawn Framing Camera. Space Sci. Rev. 163, 263–327. doi:10.1007/s11214-011-9745-4.
Sizemore, H.G., Platz, T., Schorghofer, N., Prettyman, T.H., De Sanctis, M.C., Crown, D.A., Schmedemann, N., Neesemann, A., Kneissl, T., Marchi, S., Schenk, P.M., Bland, M.T., Schmidt, B.E., Hughson, K.H.G., Tosi, F., Zambon, F., Mest, S.C., Yingst, R.A., Williams, D.A., Russell, C.T., Raymond, C.A., 2017. Pitted terrains on (1) Ceres and implications for shallow subsurface volatile distribution. Geophys. Res. Lett. 44, 6570–6578. doi:10.1002/2017GL073970.
Stein, N.T., Ehlmann, B.L., Palomba, E., De Sanctis, M.C., Nathues, A., Hiesinger, H., Ammannito, E., Raymond, C.A., Jaumann, R., Longobardo, A., Russell, C.T., 2017. The formation and evolution of bright spots on Ceres. Icarus doi:10.1016/j.icarus.2017.10.014.
Stephan, K., Jaumann, R., Zambon, F., Carrozzo, F.G., Wagner, R., Longobardo, A., Palomba, E., De Sanctis, M.C., Tosi, F., Ammannito, E., Combe, J.P., Mc Fadden, L.A., Krohn, K., Schulzeck, F., von der Gathen, I., Williams, D.A., Scully, J.E.C., Schmedemann, N., Neesemann, A., Roatsch, T., Matz, K.D., Preusker, F., Raymond, C.A., Russell, C.T., 2017. Ceres' impact craters – relationships between surface composition and geology. Icarus doi:10.1016/j.icarus.2017.10.013.
Strom, R.G., Marchi, S., Malhotra, R., 2018. Ceres and the terrestrial planets impact cratering record. Icarus 302, 104–108. doi:10.1016/j.icarus.2017.11.013.
Titus, T.N., 2015. Ceres: predictions for near-surface water ice stability and implications for plume generating processes. Geophys. Res. Lett. 42, 2130–2136. doi:10.1002/2015gl063240.
Tokar, R., Feldman, W., Prettyman, T., Moore, K., Lawrence, D., Elphic, R., Kreslavsky, M., Head III, J., Mustard, J., Boynton, W., 2002. Ice concentration and distribution near the South Pole of Mars: synthesis of odyssey and global surveyor analyses. Geophys. Res. Lett. 29, 1904. doi:10.1029/2002GL015691.
Toplis, M.J., Mizzon, H., Monnereau, M., Forni, O., McSween, H.Y., Mittlefehldt, D.W., McCoy, T.J., Prettyman, T.H., Sanctis, M.C., Raymond, C.A., Russell, C.T., 2013. Chondritic models of 4 Vesta: implications for geochemical and geophysical properties. Meteorit. Planet. Sci. 48, 2300–2315. doi:10.1111/maps.12195.
Villarreal, M.N., Russell, C.T., Luhmann, J.G., Thompson, W.T., Prettyman, T.H., A'Hearn, M.F., Küppers, M., O'Rourke, L., Raymond, C.A., 2017. The dependence of the Cerean exosphere on solar energetic particle events. Astrophys. J. 838, L8. doi:10.3847/2041-8213/aa66cd.
Wolf, D., Palme, H., 2001. The solar system abundances of phosphorus and titanium and the nebular volatility of phosphorus. Meteor. Planet. Sci. 36, 559–571. doi:10.1111/j.1945-5100.2001.tb01897.x.
Yamashita, N., Prettyman, T.H., Mittlefehldt, D.W., Toplis, M.J., McCoy, T.J., Beck, A.W., Reedy, R.C., Feldman, W.C., Lawrence, D.J., Peplowski, P.N., Forni, O., Mizzon, H., Raymond, C.A., Russell, C.T., 2013. Distribution of iron on Vesta. Meteorit. Planet. Sci. 48, 2237–2251. doi:10.1111/maps.12139.